



Formation of Massive and Wide First-star Binaries in Radiation Hydrodynamic Simulations

Kazuyuki Sugimura^{1,2,3} , Tomoaki Matsumoto⁴ , Takashi Hosokawa³ , Shingo Hirano⁵ , and Kazuyuki Omukai⁶

¹ Faculty of Science, Hokkaido University, Sapporo, Hokkaido 060-0810, Japan; sugimura@sci.hokudai.ac.jp

² The Hakubi Center for Advanced Research, Kyoto University, Sakyo, Kyoto 606-8501, Japan

³ Department of Physics, Kyoto University, Sakyo, Kyoto 606-8502, Japan

⁴ Faculty of Sustainability Studies, Hosei University, Fujimi, Chiyoda, Tokyo 102-8160, Japan

⁵ Department of Astronomy, School of Science, University of Tokyo, Tokyo 113-0033, Japan

⁶ Astronomical Institute, Graduate School of Science, Tohoku University, Aoba, Sendai 980-8578, Japan

Received 2023 July 27; revised 2023 October 11; accepted 2023 October 11; published 2023 November 30

Abstract

We study the formation of Population III stars by performing radiation hydrodynamic simulations for three different initial clouds extracted from cosmological hydrodynamic simulations. Starting from the cloud collapse stage, we follow the growth of protostars by accretion for $\sim 10^5$ yr until the radiative feedback from the protostars suppresses the accretion and the stellar properties are nearly fixed. We find that Population III stars form in massive and wide binary/small-multiple stellar systems, with masses $>30 M_{\odot}$ and separations >2000 au. We also find that the properties of the final stellar system correlate with those of the initial clouds: the total mass increases with the cloud-scale accretion rate, and the angular momentum of the binary orbit matches that of the initial cloud. While the total mass of the system in our simulations is consistent with our previous single-star formation simulations, individual masses are lower due to mass sharing, suggesting potential modification in the extent of feedback from Population III stars in the subsequent evolution of the Universe. We also identify such systems as mini-binaries embedded in a wider outer multiple-star system, which could evolve into progenitors for observed gravitational wave events.

Unified Astronomy Thesaurus concepts: [Population III stars \(1285\)](#); [Early universe \(435\)](#); [Star formation \(1569\)](#)

1. Introduction

First-generation metal-free stars, known as Population III stars, are believed to have appeared at redshifts of $z \sim 20\text{--}30$ as the first sources of light in the history of the Universe (e.g., Couchman & Rees 1986; Tegmark et al. 1997; Abel et al. 2002; Bromm et al. 2002; see also Glover 2013; Greif 2015; Klessen & Glover 2023 for a recent review). Their formation proceeds as follows: first, a small embryonic protostar forms as a result of the gravitational collapse of clouds at the center of minihalos ($10^5\text{--}10^6 M_{\odot}$) (e.g., Omukai & Nishi 1998; Yoshida et al. 2008), and then it continues to grow by accretion (e.g., Omukai & Palla 2003; Tan & McKee 2004) until the radiative feedback from the protostar eventually quenches the accretion (e.g., Omukai & Inutsuka 2002; McKee & Tan 2008; Hosokawa et al. 2011, 2016, hereafter H16; Stacy et al. 2012).

Previous numerical studies that followed the growth of embryonic Population III stars up to the end of the accretion (e.g., Hosokawa et al. 2011; Stacy & Bromm 2013; Susa 2013; Hirano et al. 2014; Susa et al. 2014; Hirano et al. 2015; Stacy et al. 2016; H16) demonstrate that Population III stars tend to be more massive than predicted from the present-day Salpeter-like initial mass function (IMF). This allows Population III stars to play crucial roles in driving the subsequent cosmic evolution through various processes, such as the reionization of the intergalactic medium by stellar radiation (e.g., Schaerer 2002; Wise et al. 2012; Ricotti et al. 2016), the metal enrichment of the pristine gas by supernovae (e.g., Woosley

et al. 2002; Chiaki et al. 2018; Abe et al. 2021), and the seeding of supermassive black hole (BH) progenitors (e.g., Alvarez et al. 2009; Jeon et al. 2012).

Observations show that massive stars are predominantly in multiple systems in the nearby Universe (e.g., Duchêne & Kraus 2013). If this is also the case in the early Universe, massive Population III stars would also be in multiples. In this case, the mass reservoir in the parental cloud will be shared among forming stars and the individual stellar masses will decrease. Such Population III binaries are attracting attention as they may later evolve into binary BHs detectable by gravitational waves (e.g., Kinugawa et al. 2014; Abbott et al. 2016; Hartwig et al. 2016; Liu & Bromm 2021; Tanikawa et al. 2021, but see also Belczynski et al. 2017) or the first X-ray binaries, which are important heating sources of the intergalactic medium and should be constrained by future 21 cm line observations (e.g., Dewdney et al. 2009; Mirabel et al. 2011). The X-ray background can also change the mode of Population III star formation (e.g., Ricotti 2016; Park et al. 2021a, 2021b, 2023).

On the theoretical side, seminal works found that Population III stars in fact end up in multiple star systems, by way of numerical simulations using particle-based codes (Stacy & Bromm 2013; Susa 2013; Susa et al. 2014; Stacy et al. 2016). In those calculations, however, protostellar feedback may have been underestimated because the density-dependent resolution of the particle-based codes was insufficient to directly follow the propagation of the ionizing radiation in the low-density polar regions around each protostar (Susa 2013).

Later, in Sugimura et al. (2020) (hereafter Paper I), we confirmed that Population III stars do form in a multiple stellar system by performing a simulation with a newly developed



Original content from this work may be used under the terms of the [Creative Commons Attribution 4.0 licence](#). Any further distribution of this work must maintain attribution to the author(s) and the title of the work, journal citation and DOI.

radiation hydrodynamic (RHD) code, SFUMATO-RT, which employs the adaptive mesh refinement (AMR; Berger & Olinger 1984; Berger & Colella 1989) and the adaptive ray-tracing (ART; Abel & Wandelt 2002) techniques to accurately follow the ionizing radiation from multiple protostars. In that work, the formation of multiple protostars by gas fragmentation and their long-term evolution are followed until the radiation feedback terminates the accretion, thereby fixing the stellar properties.

Quite recently, other groups have also performed similar simulations using other AMR codes (Latif et al. 2022; Park et al. 2023) and a moving mesh code (Jaura et al. 2022) with different radiation transfer modules. While all groups agree on the formation of multiple stars, there is a discrepancy in the effectiveness of radiation feedback. Jaura et al. (2022) argued that the trapping of ionizing radiation near protostars significantly weakens the radiative feedback unlike in the other simulations where efficient feedback is observed. The cause of this discrepancy is still unclear and further investigation is needed.

In Paper I, our simulation was limited only to a single case, despite the known diversity of the birth environments (e.g., Hirano et al. 2014). We could not discuss such statistics as the relation between the final stellar mass and the natal cloud properties found in 2D simulations (Hirano et al. 2014). Furthermore, in Paper I, we just focused on presenting the overall evolution and the nature of the resulting stellar system, leaving the analysis of the detailed physical process to future work.

In this paper, we simulate Population III star formation in three different clouds extracted from cosmological simulations, using the same code as in Paper I. Among the three clouds studied, two are new cases, while the one is the same as that already presented in Paper I. Based on the results, we examine the relation between the properties of the final stellar systems, such as the total mass and binary separation, and those of the natal clouds. We also identify and describe in detail some interesting phenomena that can play important roles in Population III star formation.

The rest of this paper is organized as follows. In Section 2, we describe our numerical methods in detail. In Section 3, we present our simulation results, from which we then investigate relations between the stellar system and natal clouds in Section 4. In Section 5, we discuss the role of radiative feedback and the numerical resolution effects. We conclude the paper in Section 6. The appendices provide a detailed description of simulation methods and a supplementary analysis of circumstellar disks in our simulations.

2. Numerical Methods

2.1. SFUMATO-RT

Our RHD code SFUMATO-RT has been developed to follow Population III star formation and was first used in Paper I. The code is an extended version of an AMR self-gravitational magnetohydrodynamic (MHD) code SFUMATO (Matsumoto 2007; Matsumoto et al. 2015), with the addition of new modules to solve the nonequilibrium chemistry and thermodynamics of primordial gas under the influence of radiation from multiple protostars (see Sadanari et al. 2021; Kimura et al. 2023; Sadanari et al. 2023, for other extensions).

2.1.1. Hydrodynamics

We use SFUMATO's modules to solve hydrodynamics with self-gravity and sink particles that represent accreting protostars. We do not use the MHD module since we ignore magnetic fields in this work.

The basic equations of hydrodynamics are

$$\frac{\partial \rho}{\partial t} + \nabla \cdot (\rho \mathbf{v}) = 0, \quad (1)$$

$$\rho \frac{\partial \mathbf{v}}{\partial t} + \rho (\mathbf{v} \cdot \nabla) \mathbf{v} = -\nabla P + \rho \mathbf{g}, \quad (2)$$

$$\frac{\partial e}{\partial t} + \nabla \cdot [(e + P)\mathbf{v}] = \rho \mathbf{v} \cdot \mathbf{g} + \Gamma - \Lambda, \quad (3)$$

$$P = (\gamma - 1)e, \quad (4)$$

where ρ is the mass density, \mathbf{v} the velocity, P the pressure, \mathbf{g} the gravitational acceleration, Γ the heating rate, Λ the cooling rate, and γ the adiabatic exponent. The mass density and pressure are related to the number density of hydrogen atoms n_{H} as $\rho = n_{\text{H}} \mu m_{\text{p}}$ and $P = n_{\text{H}} \sum_i y(i) k_{\text{B}} T$, respectively, with μ the mean molecular weight per hydrogen atom, T the temperature, m_{p} the proton mass, k_{B} the Boltzmann constant, and $y(i)$ the chemical abundances defined as the abundance ratio of species i to the hydrogen nuclei. We determine Γ , Λ , γ , and μ from T and $y(i)$ (see, e.g., Omukai & Nishi 1998). The chemical and thermal model is described in Section 2.1.2. In this work, we use the hydrodynamical scheme with second-order accuracy in space and time.

We consider both the self-gravity of the gas and the gravity of the sink particles. The total gravitational acceleration is given by

$$\mathbf{g} = -\nabla \Phi + \sum_i \mathbf{g}_{\text{sink},i}, \quad (5)$$

where Φ is the gravitational potential of the gas and $\mathbf{g}_{\text{sink},i}$ is the gravitational acceleration due to the i th sink particle. Using the multigrid solver, we obtain Φ from the Poisson equation,

$$\nabla^2 \phi = 4\pi G \rho, \quad (6)$$

with Newton's gravitational constant G . As for $\mathbf{g}_{\text{sink},i}$, we directly evaluate Newton's inverse-square law,

$$\mathbf{g}_{\text{sink},i} = -\frac{G M_i (\mathbf{x} - \mathbf{x}_i)}{|\mathbf{x} - \mathbf{x}_i|^3}, \quad (7)$$

where \mathbf{x} and \mathbf{x}_i are the positions of the gas and the i th particle, respectively.

Using the sink particle technique, we mask the neighborhoods of protostars with extremely short timescales to perform long-term simulations until the end of the accretion phase. Below, we briefly describe the implementation of sink particles in SFUMATO and refer the reader to Matsumoto et al. (2015) for details.

We create a new sink particle in a cell that satisfies the following conditions (Federrath et al. 2010):

- (i) The density is higher than the sink threshold density n_{sink} .
- (ii) The cell is a local minimum of gravitational potential Φ .
- (iii) All the eigenvalues of the symmetric parts of the velocity gradient tensor $\nabla_i v_j$ are negative.
- (iv) The total energy of the gas within the sink radius r_{sink} is negative ($E_{\text{thermal}} + E_{\text{kin}} + E_{\text{grav}} < 0$).

Around each sink particle, we define a virtual sphere with the radius r_{sink} (also called the sink sphere), which is used for the following purposes. First, the sink particle accretes the gas from the cells inside the sink sphere if the density exceeds n_{sink} until the excess disappears. Second, the sink gravity is weakened inside the sink sphere. Finally, two sink particles merge when their sink spheres overlap. In our fiducial runs, we set $r_{\text{sink}} = 64 \text{ au}$ (16 times the minimum cell size) and $n_{\text{sink}} = 2 \times 10^{11} \text{ cm}^{-3}$, as described in Section 2.3.

The AMR technique allows us to follow fine structures near multiple protostars at a relatively low computational cost. We refine the cells so that the local Jeans length is resolved with at least N_J cells. In this work, we set $N_J = 16$, which is much higher than the so-called Truelove condition $N_J \geq 4$ (Truelove et al. 1997) for avoiding artificial fragmentation. Although it has recently been claimed that higher resolution ($N_J \gtrsim 30$) is needed to follow the turbulence amplification associated with gravitational collapse (Federrath et al. 2011; Higashi et al. 2021, 2022), we adopt the above value to perform our simulations until the end of the accretion phase.

2.1.2. Nonequilibrium Chemistry and Thermodynamics

One of the major new additions of SFUMATO-RT to SFUMATO is a module for the nonequilibrium chemistry and thermodynamics of the primordial gas, which is essential to simulate Population III star formation with realistic thermal evolution. We consider the chemical reactions among six species, H^+ , H , H_2 , H^- , H_2^+ , and e^- , assuming that all the helium is neutral. To update $y(i)$ and T consistently, we solve the coupled equations for the chemical and temperature evolution, adopting an implicit method for numerical stability. Our chemical and thermal models are summarized in Appendix A.

In short, we consider all the chemical reactions and cooling and heating processes that are relevant in the density range of $n_{\text{H}} < 10^{13} \text{ cm}^{-3}$, as in H16. Major chemical reactions include the H^- -channel H_2 formation, the three-body H_2 formation, the collisional dissociation and the photodissociation of H_2 , the collisional ionization and the photoionization of H , and the radiative recombination of H^+ . Major cooling and heating processes include the H_2 line cooling with line-trapping effect, the $\text{H Ly}\alpha$ cooling, the H^- free-bound cooling, the H free-free cooling, the H free-bound cooling, the chemical cooling/heating, and the adiabatic compression heating and expansion cooling.

Inside sink spheres, we solve the nonequilibrium chemistry and thermodynamics as in the normal cells, but with neglected coupling to the radiation to avoid artificial enhancement of radiative feedback. We adopt this approach to prevent potential numerical artifacts arising from discontinuities between the interior and exterior of sink spheres. The radiation transfer model is described in the next section.

2.1.3. Radiation

Another feature of SFUMATO-RT is the addition of a radiation module to handle the radiation from multiple sources. Here we consider three types of radiation: extreme-ultraviolet radiation (EUV; $h\nu > 13.6 \text{ eV}$), which photoionizes H ; far-ultraviolet (FUV) radiation ($11.2 \text{ eV} < h\nu < 13.6 \text{ eV}$), which photodissociates H_2 ; and near-infrared (NIR) radiation ($h\nu < 11.2 \text{ eV}$), which photodetaches H^- . We solve the

radiation transfer for the EUV and FUV, while the NIR is assumed to be optically thin, which is a good approximation in the accreting envelope (see Hosokawa et al. 2011). Below, we describe the protostellar model, the radiation transfer method, the sink-scale treatments, and the coupling with chemistry and thermodynamics in this order.

Protostellar model—We assign the radiative properties of Population III protostars by the tabulated results of one-dimensional (proto)stellar evolution calculations under constant accretion rates (Hosokawa & Omukai 2009; Hosokawa et al. 2010). The table gives the luminosity L_* and stellar radius R_* for a given set of the stellar mass M and accretion rate \dot{M} . From L_* and R_* , we derive the effective temperature T_{eff} , EUV emissivity S_{EUV} , and FUV emissivity S_{FUV} , assuming a blackbody spectrum (see Appendix B for more details). We also obtain the optically thin H^- photodetachment rate as a function of the distance from the protostar.

Following H16, we average the accretion rate over 300 yr to account for the timescale of gas transport through unresolved parts of the accretion disk. We only consider radiation from protostars more massive than $M_{\text{rad,min}} = 5 M_{\odot}$ to save computational cost since the UV emissivities before the onset of the Kelvin–Helmholtz contraction are extremely small (see Appendix B).

Our protostellar radiation model neglects the dependence of stellar properties on the accretion history. H16 found a case in which the intermittent plunge of fragments causes accretion bursts, and thus the accretion history matters indeed. In our simulations, however, we expect the dependence on the accretion history to be less important because the gas is mostly supplied to protostars by continuous gas accretion from the circumstellar disks, with modest modulation due to binary interactions, except in early phases when radiation feedback is negligible.

Radiative transfer method—To solve the transfer of EUV and FUV radiation, we trace rays from each source by way of the ART method (Abel & Wandelt 2002; Krumholz et al. 2007; Wise & Abel 2011; Kim et al. 2017; Rosen et al. 2017). Below, we briefly explain our radiative transfer method and refer the readers to the literature above for details about the ART method. We present our specific implementation to SFUMATO-RT in Appendix C.

For the EUV radiation, we trace the direct photons from each protostar considering the attenuation due to photoionization, with the diffuse recombination photons treated by the on-the-spot approximation, following H16. At a distance r from a radiation source, the optical depth is obtained by the integration along a ray as

$$\tau_{\text{EUV}} = \int_{r_{\text{sink}}}^r \sigma_{\text{pi}} n_{\text{H}} y(\text{H}) dr', \quad (8)$$

with σ_{pi} the effective photoionization cross section depending on the source's spectrum. We omit the attenuation within the sink sphere in Equation (8) by setting the lower bound of the integration to r_{sink} , and separately consider the sink-scale attenuation, as described below. With τ_{EUV} along each ray, we evaluate the EUV photoionization rate in each cell as

$$k_{\text{pi}} = \sigma_{\text{pi}} \frac{S_{\text{EUV}}}{4\pi r^2} \langle e^{-\tau_{\text{EUV}}} \rangle_{\text{cell}}, \quad (9)$$

and the EUV photoheating rate as

$$\Gamma_{\text{pi}} = \sigma_{\text{pi}} \epsilon_{\text{EUV}} \frac{S_{\text{EUV}}}{4\pi r^2} \langle e^{-\tau_{\text{EUV}}} \rangle_{\text{cell}}, \quad (10)$$

where $\epsilon_{\text{EUV}} = \langle h\nu - 13.6 \text{ eV} \rangle$ is the mean energy deposited in the gas per photoionization. The bracket $\langle \rangle_{\text{cell}}$ denotes the average over the rays penetrating the cell (e.g., Wise & Abel 2011). If rays from multiple sources reach the cell, we take the sum of each source's contribution.

For the FUV radiation, instead of the optical depth, we evaluate the H_2 column density as

$$N_{\text{H}_2} = \int_{r_{\text{sink}}}^r n_{\text{H}} y(\text{H}_2) dr' \quad (11)$$

along a ray to model the self-shielding effect. We then estimate the FUV photodissociation rate as

$$k_{\text{pd}} = \sigma_{\text{pd}} \frac{S_{\text{FUV}}}{4\pi r^2} \langle f_{\text{shield}} \rangle_{\text{cell}}, \quad (12)$$

with the effective photodissociation cross section σ_{pi} and the self-shielding factor f_{shield} . For this work, we adopt the widely used formula $f_{\text{shield}} = \min[1, (N_{\text{H}_2}/10^{14} \text{ cm}^{-2})^{-0.75}]$ from Draine & Bertoldi 1996, although more elaborate ones have recently been proposed (e.g., Wolcott-Green & Haiman 2019).

In the ART framework, to achieve the desired directional resolution, we split rays hierarchically using the HEALPix library (Górski et al. 2005). At each ray level l_{ray} , the spherical 4π solid angle is sampled by $N_{\text{ray}} = 12 \times 4^{l_{\text{ray}}}$ rays that cover equal-area pixels with $4\pi/N_{\text{ray}}$. We start ray tracing from each sink particle by injecting $N_{\text{ray,ini}} = 12 \times 4^{l_{\text{ray,ini}}}$ rays at the initial ray level $l_{\text{ray,ini}} = 3$. While tracing the rays, we split a parent ray into four daughter rays at one higher HEALPix level to ensure that at least $N_{\text{ray,min}}$ rays pass through each cell surface. In this study, we use $N_{\text{ray,min}} = 3$, following the resolution study of Krumholz et al. (2007). We have examined the effect of this choice by performing a test run with $N_{\text{ray,min}} = 5$ and have confirmed that its effect on the total mass evolution is insignificant, at least until the middle phases of star formation. We randomly rotate the HEALPix orientation at each ART step to mitigate artifacts due to insufficient discretization (Krumholz et al. 2007).

Sink-scale treatments—We need separate treatments for radiation rays inside sink spheres, where the gas distribution is not resolved and can be artificial. For example, the inner geometrically thin part of an accretion disk, in reality, may be artificially thick in simulations due to the softening of the protostar's gravity inside the sink sphere.

To account for the shielding of central radiation by unresolved parts of a disk inside a sink sphere, we allow only rays with elevation angles greater than the disk thickness to cross the sink sphere. Here, we measure the disk thickness at the sink radius, assuming that the aspect ratio is an increasing function of the radius.⁷ In practice, when a ray crosses a sink sphere, we check whether the density is higher than the disk threshold density $n_{\text{disk}} = 10^{-2} n_{\text{sink}}$. If this is the case, assuming that the ray is traveling in the direction shielded by the disk, we terminate the ray before it has any effect on the surrounding gas. We have confirmed that the effect of radiative feedback is not sensitive to the particular choice of n_{disk} , by comparing

axisymmetric test simulations of accreting protostars with fiducial n_{disk} and 10 times larger n_{disk} .

In addition to the disk shielding, we model the EUV absorption in the polar directions following H16. For each ray emitted from a protostar, we measure the density of the cell where the ray crosses the sink sphere and check whether the Strömgren radius r_{strm} for a homogeneous medium with this density (the temperature is assumed to be $T = 4 \times 10^4$ K, which is a typical value for H II regions around Population III stars) is smaller than the sink radius. If this is the case, we assume that the EUV is consumed inside the sink sphere and set a very large τ_{EUV} (effectively no EUV effect remains). Of course, the assumption of a homogeneous medium inside the sink sphere is not very accurate: the density along the ray increases inward in the case of a spherical free-falling flow as $\propto r^{-3/2}$; conversely, the density may decrease in the case that the polar regions are cleared due to the centrifugal force.

Alternatively, Jaura et al. (2022) distributed photons at the center of sink spheres and solved the radiation transfer inside those spheres. As a result, the effect of radiative feedback is strongly suppressed in their simulations, as all photons are absorbed by the thick disks inside the sink spheres. At present, the precise gas distributions surrounding protostars are unknown, introducing uncertainties into the sink-scale radiation model used in star formation simulations. We expect that high-resolution RHD simulations, capable of resolving the star-disk interfaces and the inner part of accretion disks (see Kimura et al. 2023), are valuable in addressing this matter.

Coupling with chemistry—In each ART step, we trace rays on the fixed background of the density and chemical composition. We then update the chemistry and thermodynamics under the fixed radiation field reconstructed from the result of the previous ray tracing. We perform the ART plus chemistry/thermodynamics sub-cycles n_{sub} times per hydrodynamic step. In this study, we choose $n_{\text{sub}} = 2$ so that the maximum propagation speed of the dissociation and ionization fronts in the sub-cycles (two cells per one hydrodynamic step) is faster than that associated with the hydrodynamic flows (one cell per one hydrodynamic step). As a result, we expect that the fronts can (in principle) reach the positions determined by the ionization/recombination and dissociation/formation equilibria, respectively.

2.2. Initial Conditions

We extract primordial star-forming clouds from cosmological 3D SPH/ N -body simulations (Hirano et al. 2014, 2015) as the initial conditions for our 3D AMR RHD star formation simulations. Specifically, we remap particle-based simulation data of primordial clouds early in the collapse phase (when the central density reaches 10^6 cm^{-3}) to Cartesian grids to generate the initial conditions.

Table 1 summarizes the properties of the three clouds studied in this paper. These clouds have a range of initial cloud-scale accretion rate \dot{M}_{cloud} spanning from 10^{-3} to $10^{-2} M_{\odot}/\text{yr}$. We give names to these clouds based on their respective cloud-scale accretion rates: high-, intermediate-, and low- \dot{M} clouds. The intermediate- \dot{M} cloud is the same one studied in Paper I. Our selection of clouds with different \dot{M}_{cloud} enables us to study a wide variety of Population III star-forming environments, as \dot{M}_{cloud} is known to correlate with the final stellar mass (Hirano et al. 2014, H16).

⁷ It scales as $H/R = (c_s/\Omega)/R \sim R^{1/2}$ in a vertically hydrostatic isothermal disk.

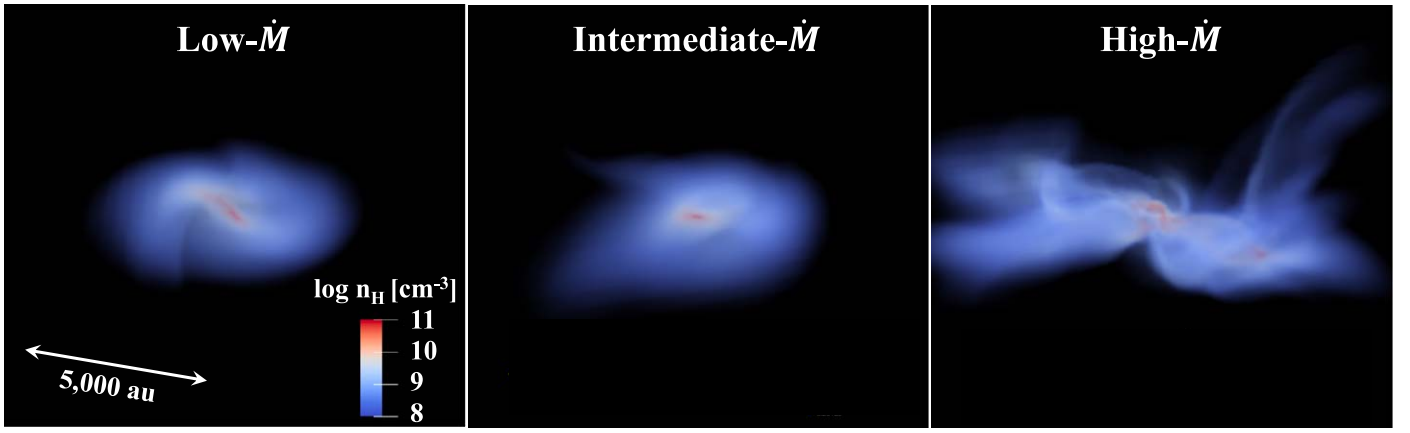


Figure 1. The state of the cloud cores just before the formation of the first protostars. We show the density rendered image for the low- \dot{M} (left), intermediate- \dot{M} (middle), and high- \dot{M} (right) clouds.

Table 1
Summary of Initial Clouds

Cloud ^a (1)	z_{col} (2)	$M_{\text{DM,halo}} (M_{\odot})$ (3)	R_{cloud}^b (pc) (4)	M_{cloud}^c (M_{\odot}) (5)	\dot{M}_{cloud}^d ($M_{\odot} \text{ yr}^{-1}$) (6)	λ_{cloud}^e (7)
Low \dot{M}	18	4.2×10^5	0.08	130	7.6×10^{-4}	0.24
Intermediate \dot{M}	24	2.5×10^5	0.32	860	2.2×10^{-3}	0.22
High \dot{M}	16	8.3×10^5	0.25	970	5.2×10^{-3}	0.14

Notes. Column (1): cloud name, column (2): collapse redshift, column (3): dark matter mass of the minihalo, column (4): cloud radius, column (5): gas mass of the cloud, column (6): cloud-scale accretion rate, column (7): cloud spin parameter.

^a The high- \dot{M} , intermediate- \dot{M} , and low- \dot{M} clouds in this paper are identical to the clouds in Cases A, C, and D in H16, respectively. See Hirano et al. (2015) and H16 for further information about the cloud properties. The intermediate- \dot{M} cloud also corresponds to the cloud studied in Paper I. All cloud parameters are evaluated when the central density reaches $n_{\text{H}} = 10^7 \text{ cm}^{-3}$.

^b The radius at which the ratio of the enclosed mass to the local Jeans mass takes its maximum value (see Hirano et al. 2015).

^c The gas mass within R_{cloud} .

^d The accretion rate through the spherical surface at R_{cloud} .

^e The spin parameter defined as $\lambda_{\text{cloud}} = J_{\text{cloud}} / \sqrt{2 G M_{\text{cloud}}^3 R_{\text{cloud}}}$, with J_{cloud} the angular momentum within R_{cloud} (see Hirano et al. 2015).

After the onset of our re-simulation, the pre-stellar collapse continues until the first protostar, i.e., sink particle, appears around the cloud center. Here, we show the state of the clouds just before the first protostar formation by the 3D rendering of the central cores in Figure 1 and the 1D radial profiles of the entire clouds in Figure 2.

Figure 1 depicts the diverse morphology of central cores in the three clouds. The cores in the low- and intermediate- \dot{M} cases are rotating and have disk-like shapes, with the former having a noticeable bar-spiral structure. In contrast, the core in the high- \dot{M} case is turbulent and filamentary in shape. Those cores can be considered as the initial states of Population III star formation via accretion, as described in Section 3.

As seen in the density and temperature profiles shown in the top two panels of Figure 2, the clouds undergo the so-called runaway collapse, with a slightly increasing temperature characterized by an effective polytropic index of $\gamma_{\text{eff}} \approx 1.1$ (Omukai & Nishi 1998). The third panel presents the inflow rates, \dot{M} , at a given radius, which are overall consistent with the values of \dot{M}_{cloud} (Table 1). Note, however, that those two quantities do not exactly match at either radius because the measurements are taken at different epochs while \dot{M} gradually increases over time (Hirano et al. 2015). The bottom two panels show the degree of rotational support $f_{\text{Kepler}} = \Omega / \Omega_{\text{Kepler}}$ and

the turbulent Mach number $\mathcal{M}_{\text{turb}} = v_{\text{turb}} / c_s$, where Ω_{Kepler} is the Keplerian angular velocity and v_{turb} is the turbulent velocity. The high- \dot{M} case exhibits stronger turbulence than the two other cases, with a lower degree of rotational support. The initial states of the clouds before the accretion phase are closely linked to the properties of final Population III systems, as discussed in Section 4.

2.3. Simulation Setup

We perform three runs, namely, high, int, and low runs, corresponding to the high- \dot{M} , intermediate- \dot{M} , and low- \dot{M} clouds in Section 2.2, respectively. Table 2 summarizes our simulation setup and results.

We set the side length of our simulation box to 2.6 or 5.2 pc to encompass the collapsing region of the cloud with sufficient margin. The minimum cell size at the highest AMR level is $\Delta x_{\text{min}} = 4 \text{ au}$, with the sink radius of $r_{\text{sink}} = 64 \text{ au}$, equivalent to 16 times Δx_{min} . Such a large number of cells per sink radius is necessary to resolve geometrically thin accretion disks with a thickness of $\sim 10 \text{ au}$ around the sink radius: inadequate resolution would artificially align the disk to one of the Cartesian axes since the gas can be advected only through the cell surfaces in grid simulations. We adopt a sink threshold density of $n_{\text{sink}} = 2 \times 10^{11} \text{ cm}^{-3}$, ensuring that the

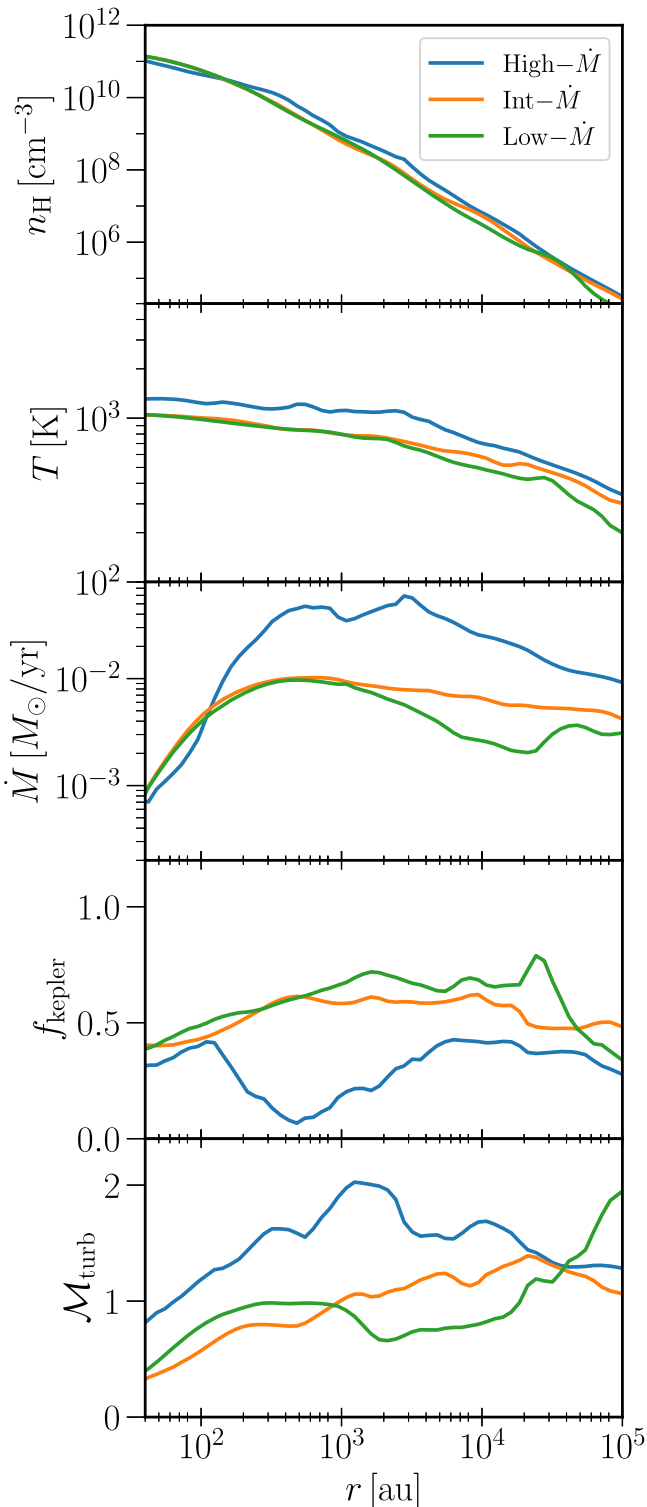


Figure 2. The radial profiles of physical quantities just before the first protostar formation for the three clouds (low- \dot{M} , green dotted; intermediate- \dot{M} , orange dashed; and high- \dot{M} , blue solid). From top to bottom, the density n_{H} , temperature T , inflow rate \dot{M} , degree of rotational support f_{kepler} , and turbulent Mach number $\mathcal{M}_{\text{turb}}$ are plotted.

corresponding Jeans length matches the sink diameter of $2 r_{\text{sink}}$ (with $T = 10^3$ K, representing a typical temperature of neutral gas at density n_{sink}). We terminate our simulations at $\Delta t = 80,000$ or $100,000$ yr, when accretion is quenched by radiation feedback and the total mass is almost fixed.

3. Numerical Results

In this section, we present our simulation results. We first describe the overall evolution in Section 3.1, and then examine noteworthy interesting phenomena in detail in Section 3.2.

3.1. Overall Evolution

First, we provide an overview of the star formation process in the three clouds simulated in this paper. To visually depict the evolution, we show the face-on slice density in Figure 3 and the edge-on slice temperature in Figure 4 for the low- (top), intermediate- (middle), and high- \dot{M} (bottom) runs at different evolutionary stages. Specifically, we plot the snapshots at $\Delta t = 3000$ yr (left), $10,000$ yr (middle), and $30,000$ yr (right), with Δt being the time since the first protostar formation. In all three cases, multiple protostars are formed as a result of the initial disk fragmentation (Figure 3, left), in agreement with previous simulations of Population III star formation that followed the early phase (e.g., Machida et al. 2008b; Clark et al. 2011; Greif et al. 2011; Smith et al. 2011; Greif et al. 2012; Hirano & Bromm 2017; Sharda et al. 2019; Susa 2019). Subsequently, the protostars grow in mass via gas accretion (Figure 3, middle) until the radiation feedback quenches it (Figure 4, right). The resulting stellar system is either a binary of two stars (in the low- and high- \dot{M} cases) or a binary of a single star and a mini-triplet system (in the intermediate- \dot{M} case), as shown in Figure 3 (right).

To see the evolution, we plot the mass (top), accretion rate (middle), and separation of selected pairs (bottom) of protostars, i.e., sink particles, in Figure 5. As described above, multiple protostars are formed by the initial disk fragmentation ($\Delta t \lesssim 5000$ yr), grow in mass via gas accretion ($\Delta t \sim$ a few $\times 10,000$ yr), and finally cease to grow due to radiative feedback, with the accretion rates dropping to such a low level that the total masses are almost fixed at the end of the simulations ($\Delta t = 80,000$ or $100,000$ yr). Many protostars disappear in mergers induced by unstable gravitational interaction in few-body systems, and only two to four stars survive at the end of the simulations.

We summarize the properties of the final stellar systems in Table 2. The total masses are $M_{\text{tot}} = 100\text{--}500 M_{\odot}$, with increasing masses toward higher cloud-scale accretion rates (e.g., Hirano et al. 2014). The number of surviving protostars is $N_{\text{sink}} = 2$ or 4 . The masses of the most and the second most massive stars in the system, M_1 and M_2 , respectively, are all quite large ($>30 M_{\odot}$) with the most massive one reaching even $370 M_{\odot}$. The mass ratio of $q_{12} = M_2/M_1$ is around $0.3\text{--}0.8$, which means moderate mass hierarchy. The semimajor axis of their binary orbits is $a_{12} = 2 \times 10^3\text{--}2 \times 10^4$ au at the end of the simulations. In all cases, the final outcomes are widely orbiting (>2000 au) massive ($>30 M_{\odot}$) multiple stellar systems.

Although only with a very small sample size, it is worth comparing the distribution of our binary properties with the binary statistics in the literature, which have been used to estimate the rate of binary BH mergers. Our sample of massive binaries, characterized by large primary masses ($M_1 \gtrsim 60 M_{\odot}$), wide orbits ($a_{12} \sim 1000\text{--}10,000$ au), and moderate mass ratios ($q_{12} \sim 0.3\text{--}0.8$), roughly agrees with the binary statistics of Liu et al. (2021, see their Figure 9), who considered the effect of orbital expansion due to the conservation of angular momentum. The statistics of Liu et al. (2021) predict

Table 2
Summary of Fiducial Runs

Run ^a (1)	L_{box} (au) (2)	Δx_{min} (au) (3)	r_{sink} (au) (4)	Δt_{end} (yr) (5)	N_{sink} (6)	M_{tot} [M_{\odot}] (7)	M_1 (M_{\odot}) (8)	M_2 (M_{\odot}) (9)	a_{12} (au) (10)	M_{H16} (M_{\odot}) (11)
Low	2.6×10^5	4	64	10^5	2	98	64	34	8×10^3	67
Int	5.2×10^5	4	64	10^5	4	148	67	56	2×10^4	286
High	5.2×10^5	4	64	8×10^4	2	497	370	127	2×10^3	$>462^b$

Notes. Column (1): run name, column (2): side length of the simulation box, column (3): minimum cell size, column (4): sink radius, column (5): simulation duration since the first protostar formation, column (6): number of sink particles surviving until the end of the simulation, column (7): total mass of the stars, column (8): mass of the most massive star, column (9): mass of the second most massive star, column (10): semimajor axis of the orbit of the most and the second most massive stars, column (11): stellar mass in H16.

^a Low, int, and high runs are for the high- \dot{M} , intermediate- \dot{M} , and low- \dot{M} clouds in Table 1, respectively.

^b Accretion continues when H16 stops their simulation.

significantly fewer close binaries than other studies that assume simple models without the above expansion effect (e.g., Kinugawa et al. 2014; Belczynski et al. 2017).

3.2. Some Characteristic Phenomena

Next, we describe characteristic phenomena observed in our simulation runs. Some of them are common to all the runs, while others occur only in a limited run(s), partly explaining the reason for the observed similarity or diversity of the formed systems. In what follows, we describe those processes one by one in each run.

3.2.1. Low- \dot{M} Run

In the low- \dot{M} run, we identified the following two characteristic processes, both of which are also observed in the two other cases. The first is initial disk fragmentation, which seeds multiple protostars, and subsequent few-body interaction, which induces mergers between them. The second is the photoevaporation of a circumstellar disk by another protostar.

Initial disk fragmentation followed by a few-body interaction among fragments—At the end of the gravitational collapse, the first protostar appears at the center of the rotating cloud (see Figures 1 and 2). Around the protostar, an accretion disk soon forms thanks to the accumulation of the angular momentum from the rotating envelope. Since the disk is relatively massive compared with the central protostar in the early phase (see Kimura et al. 2021), the disk promptly fragments and produces two new protostars at $\Delta t \approx 2000$ and 4000 yr (Figure 5). A clump in a spiral arm (at lower-left in the upper left panel of Figure 3 at $\Delta t = 3000$ yr) will later develop into the third protostar.

After formation by the disk fragmentation, those three protostars interact with each other and two of them eventually merge, as can be seen in the top panel of Figure 6, which depicts their trajectories before and after the merger. The trajectories of the three protostars change violently since a three-body system is generally unstable. The interactions tend to be strong in the earliest phase because the protostars have similar masses and short mutual distances, comparable to the disk radius. After the merger of two protostars at $\Delta t \approx 20,000$ yr, a wide orbit eccentric binary system is left, as shown in Figure 6 (bottom).

Changing their orbits, the protostars grow in mass by gas accretion, as can be seen in Figure 5 (upper left). The accretion rate onto each protostar remains roughly constant until the merger event, where the gas in the disks is stripped away by the

gravitational interactions and the accretion rate drops suddenly (Figure 5, middle left). Photoevaporation by the central protostars causes mass loss from the accretion disk surface (see Figure 4, top right) and reduces the accretion rate even more. Around this time, the protostars left are scattered into a low-density peripheral region, and the gas supply to the disks is also quenched (see Figure 6, bottom). Although accretion is enhanced temporarily due to the perturbation by the other star on the circumstellar disk around the pericentric encounter at $\Delta t \approx 50,000$ yr (Park et al. 2023), the associated mass growth is modest.

Disk photoevaporation by a nearby protostar—After the pericentric encounter, the accretion rates soon drop again. One of the stars completes the photoevaporation of its own accretion disk and then begins to photoevaporate the disk of another nearby star. The time sequence of this *external* photoevaporation is shown in Figure 7. Soon after the photoevaporation of its own disk by the left star, the ionized region readily expands into a surrounding lower-density region and finally engulfs the disk on the right side.

We must remark that the external photoevaporation in this case does not play a significant role in setting the final stellar mass. This is because, by this time, the accretion rate has already fallen to a value too low to change the mass.

Note that such external photoevaporation is observed not only in the low- \dot{M} case, but also in all other cases. In our runs, its role in controlling the evolution of protostellar systems is limited: although this may explain peculiar late-time orbital evolution seen in the intermediate- \dot{M} case (see Section 3.2.2), it does not affect the final stellar mass significantly in any runs. External photoevaporation, however, may play an important role in setting the mass of low-mass stars that are unable to clear the disk material away by their own radiation alone. The reason that such stars are not observed in our current runs is partly due to resolution limitations. In any case, given the prevalence of external photoevaporation, its role in Population III star formation is worth further investigation. For example, in Galactic star-forming regions, photo-evaporating disks by external irradiation, also called *proplyds*, are of interest because they not only leave interesting observational tracers but also have effects on the disk evolution, including planet formation (e.g., Yorke & Welz 1996; Haworth et al. 2017).

3.2.2. Intermediate- \dot{M} Case

In the intermediate- \dot{M} case, we also observe the initial disk fragmentation followed by a few-body interaction, as well as the external disk photoevaporation. The outcome of the former

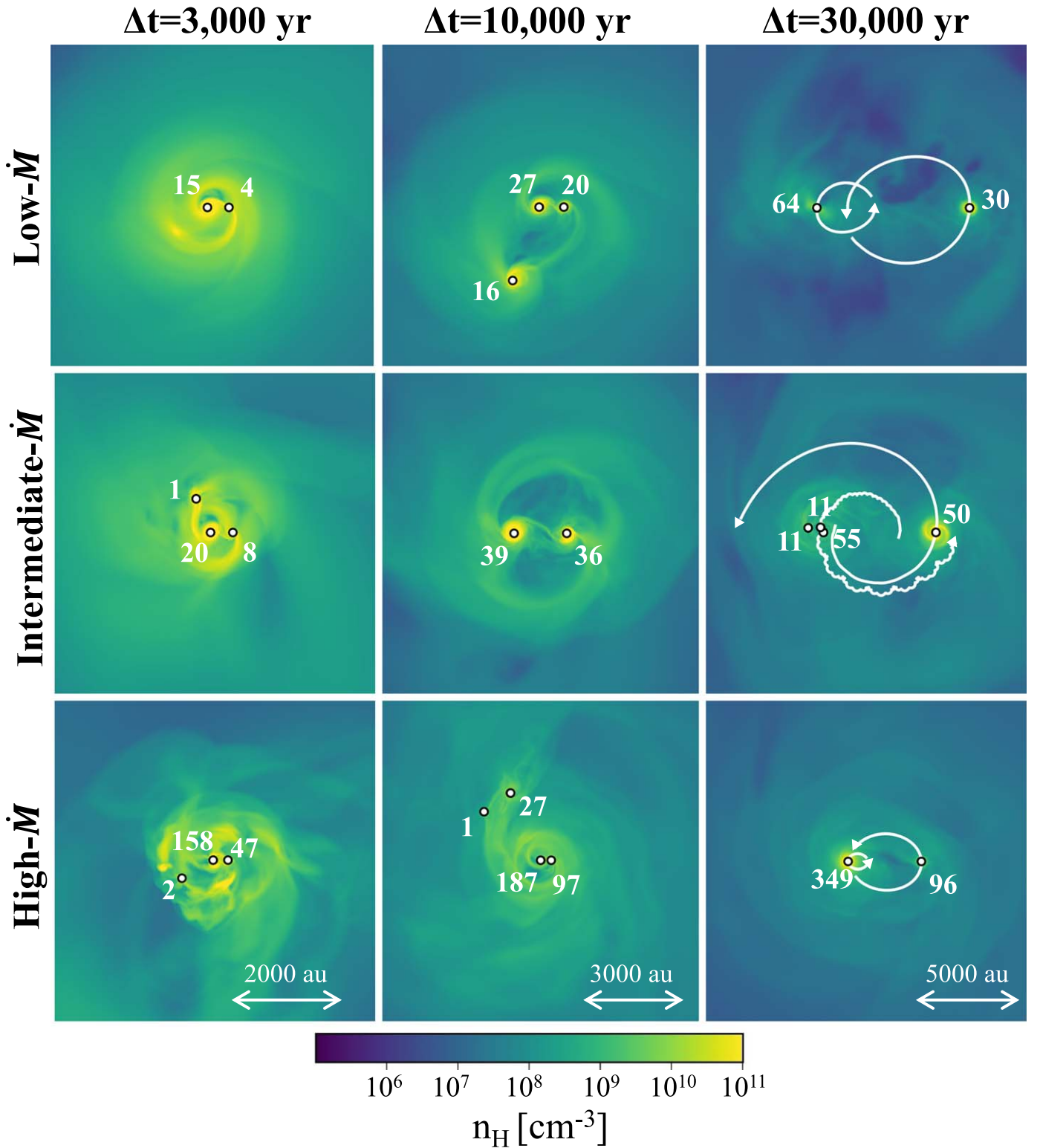


Figure 3. Face-on slice density in the low- \dot{M} (top), intermediate- \dot{M} (middle), and high- \dot{M} (bottom) cases at $\Delta t = 3000$ yr (left), 10,000 yr (middle), and 30,000 yr (right) since the first protostar formation. The projected positions of the sink particles are shown as open circles, with their masses indicated in M_{\odot} . Note that the size of the sink particles shown is larger than the actual size for better visibility. In the right column, we show the trajectories of the most and second most massive protostars.

event is, however, different here: a circular, rather than eccentric, binary system is left, unlike in the low- \dot{M} run, possibly due to the chaotic nature of few-body systems. The binary then accretes gas from the circumbinary disk (Figure 3, center) around the member stars' circumstellar disks. Eventually,

one of them fragments, leading to the formation of a mini-triplet system (Figure 3, middle right). Here, we describe those two processes specific to the intermediate- \dot{M} case.

Binary evolution by accretion from the circumbinary disk—After the initial interaction phase ($\Delta t \gtrsim 6000$ yr), the binary's

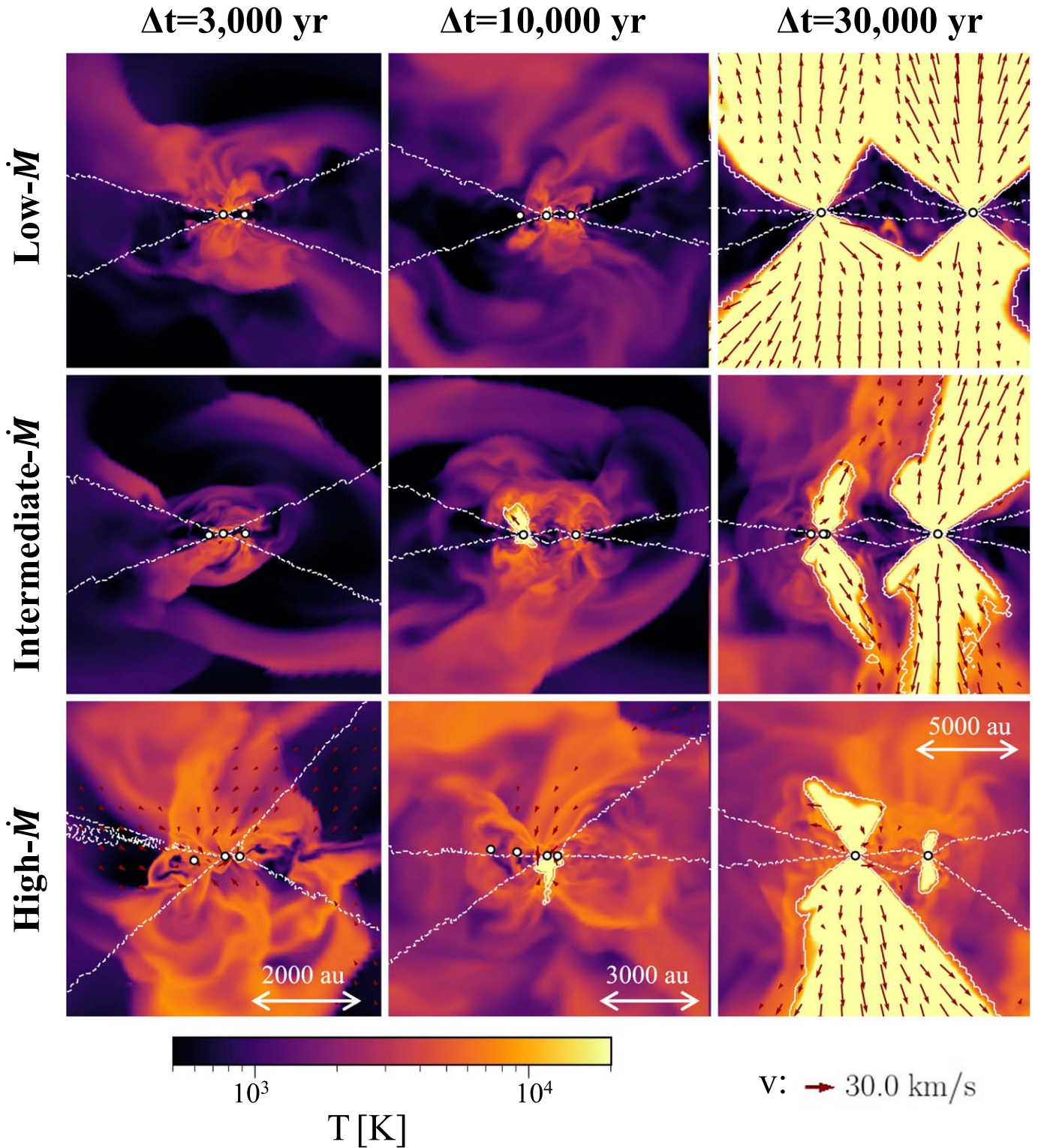


Figure 4. Same as Figure 3 but for the edge-on slice temperature. The bipolar photoionization and photodissociation fronts are demarcated with solid and dashed lines. The gas velocity is indicated by arrows whose length is proportional to its amplitude.

mass and separation significantly change, as shown in Figure 5. This is due to accretion from the circumbinary disk to the protostars through the circumstellar disks (Figure 3, center). To see this clearly, we investigate the structure of the accretion flows on the circumbinary disk scale at $\Delta t = 10,000$ yr. Figure 3 (center) illustrates the binary system with a separation of ≈ 1000 au embedded in a circumbinary disk

spanning from ≈ 2000 au to the outer radius. This configuration is also evident in the 1D surface density profile presented in Figure 18 (top) of Appendix D. Gases are transferred from the circumbinary disk to the circumstellar disk of each star through the interfaces, i.e., on the left (right, respectively) side of the left (right) star, while gaps are created on the upper and lower sides.

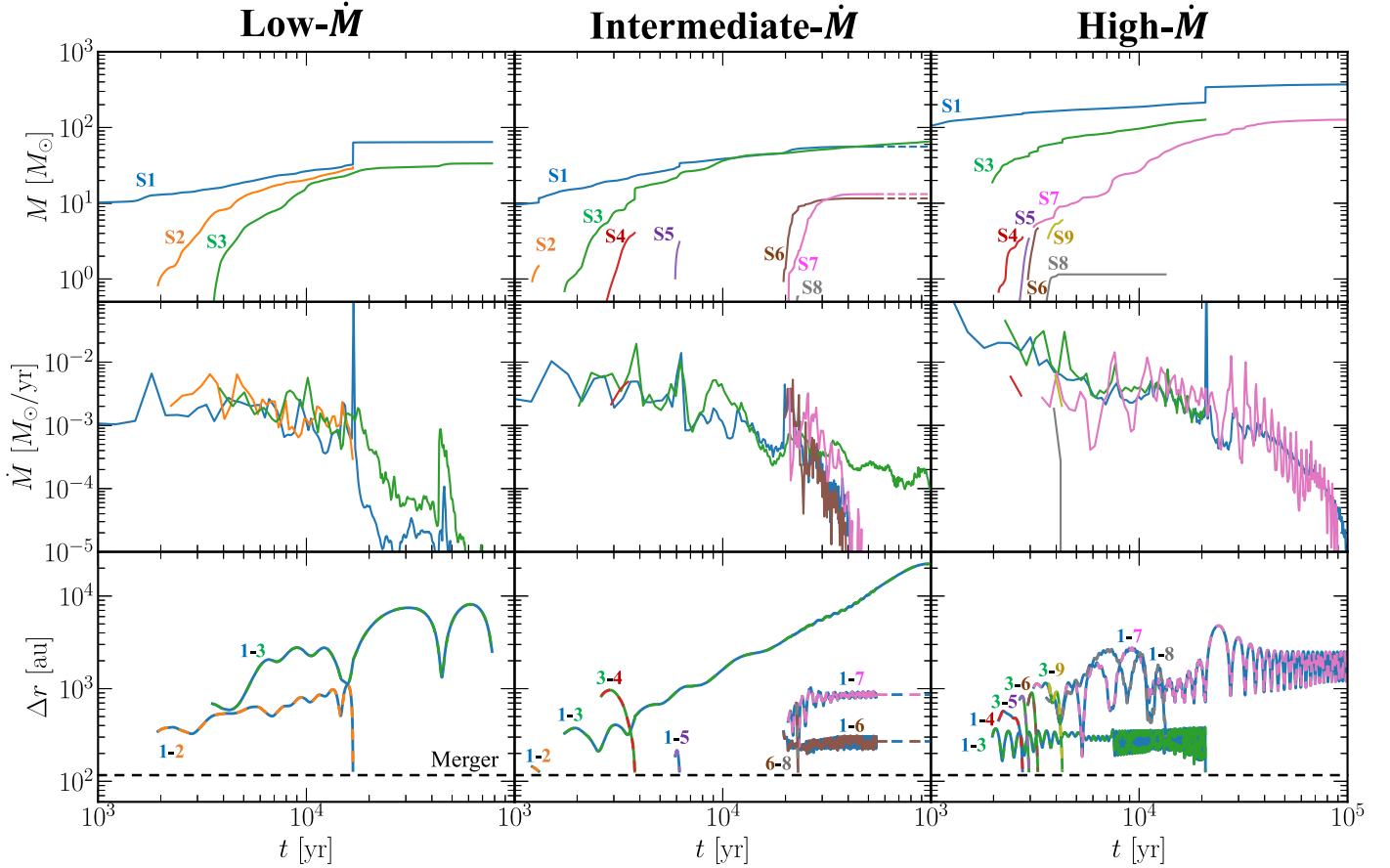


Figure 5. Evolution of protostars, i.e., sink particles, in the three clouds: from left to right columns, low-, intermediate- and high- \dot{M} (right) clouds. From top to bottom, the masses, accretion rates (averaged over 300 yr), and distances between selected pairs are plotted. In the top two panels, the same color is used for the same protostar, whose ID is indicated in the top panel, while a combination of the two colors of the member stars is used to indicate the pair in the bottom panel. The black-dashed line in the bottom panel indicates the distance below which two sink particles are assumed to merge. In the intermediate- \dot{M} case, we do not follow the individual dynamics of the mini-triplet after $t = 5.5 \times 10^4$ yr (dashed, see Paper I). In the high- \dot{M} case, the second sink particle does not appear in the plot as it merges with the first one at $\Delta t = 100$ yr, before the beginning of the plot.

The circumbinary disk rotates at a rate slightly lower than the Keplerian for the enclosed mass, i.e., the sum of protostars and gas (see the third row in Figure 18 in Appendix D for the 1D angular velocity profile). Since its specific angular momentum is higher than the binary’s orbital value, the accretion from the disk provides the binary with angular momentum. This explains the observed increase in binary separation with mass (e.g., Chon & Hosokawa 2019; Moody et al. 2019; Muñoz et al. 2019; Heath & Nixon 2020; Tiede et al. 2020).

The driving mechanism of accretion, i.e., of the angular momentum transfer, varies depending on the flow segment. In Figure 8 (top), we present the face-on view of the Toomre’s Q parameter, defined as $Q \equiv c_s \kappa / \pi G \Sigma$, with Σ the column density, $\kappa \equiv \left[(2\Omega/R) \frac{d}{dR} (R^2 \Omega) \right]^{1/2}$ the epicyclic frequency, and Ω the angular frequency around the barycenter of the binary. This parameter is an indicator of gravitational stability: a region of the disk is stable if $Q > 1$ and unstable otherwise. Figure 8 (top) shows that the circumbinary disk is marginally unstable with $Q \sim 1$ at outer radii $\gtrsim 2000$ au (also see the bottom panel of Figure 18 in Appendix D). Within the circumbinary disk, the accretion is driven by the gravitational torque exerted by spiral arms, which are continuously generated and disrupted, as is commonly assumed in 1D models of a circumstellar accretion disk (e.g., Kimura et al. 2021; Matsukoba et al. 2021). On the other hand, in the region

between the circumbinary and the circumstellar disks (≈ 1500 – 2000 au; see Figure 3, center) $Q > 1$, i.e., the gas is stable against self-gravity, suggesting that accretion is primarily driven by the torque exerted by the binary’s gravity. On the smaller scale within each circumstellar disk, the accretion is again governed by the disk’s self-gravity ($Q \sim 1$), as presented in Appendix E. The circumstellar disks have a similar structure to that of the conventional (quasi-)axisymmetric one in the literature (e.g., Hosokawa et al. 2011; H16).

The vertical structure of the disks is shown in Figure 8 (bottom). The circumbinary disk puffs up to >1000 au in the vertical direction (also see the fourth panel of Figure 18 in Appendix D) due to its weak gravity, in contrast to the thin circumstellar disks of a few hundred astronomical units (see Appendix E). At this moment, bipolar H II regions are still confined to the vicinity of the protostars and radiative feedback is insignificant (Figure 4, center; see also Appendix E).

From the analysis above, a unified picture can be drawn regarding accretion flows, which cause the binary’s mass growth, as well as orbit expansion. Accretion proceeds first from the circumbinary disk to the circumstellar disks and then to the protostars, and the mechanism of angular momentum transfer depends on the region of the flow.

Finally, we comment on a possible effect of radiative feedback on the binary orbital evolution. The increase of the binary separation can be ascribed to the accretion of high

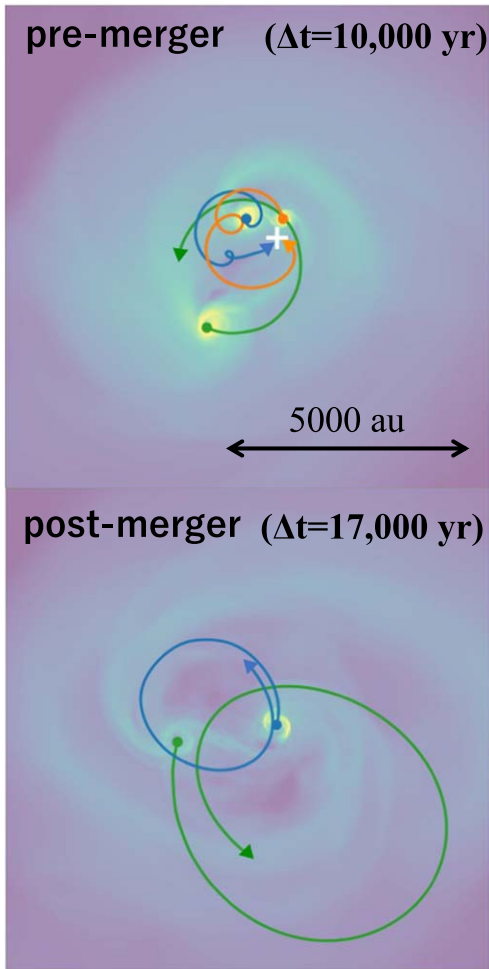


Figure 6. Trajectories of protostars before ($\Delta t = 10,000$ yr, top) and after ($\Delta t = 17,000$ yr, bottom) merger in the low- \dot{M} case. We plot trajectories on the background of a white-shaded density map. Three-body interaction induces the merger, leading to the formation of an eccentric binary. The white cross in the upper panel indicates the point of merger.

angular momentum gas during the period of $\Delta t \lesssim 30,000$ yr, where the accretion onto stars is in fact vigorous. The separation, however, continues to increase thereafter despite no significant mass growth. This requires a different explanation. One possibility is a backward/forward asymmetry in density around the star due to radiative feedback. Indeed, BHs moving in the ambient gas are known to be accelerated by such asymmetries (Park & Bogdanović 2017; Sugimura & Ricotti 2020; Toyouchi et al. 2020). Another possibility is a reduction in the gravitational pull on the binary stars due to the photoevaporative loss of gas in the region between the binary. The effect of radiative feedback on orbital evolution merits further investigation.

Late-time disk fragmentation and acceleration of photoevaporation—During binary accretion, one of the circumstellar disk fragments forms a mini-triplet system at $\Delta t = 20,000$ yr (see Figure 5). The state of the disk before ($\Delta t = 18,000$ yr) and after ($\Delta t = 30,000$ yr) fragmentation is shown in Figure 9. The fragmentation of a spiral arm in the circumstellar disk (Figure 9, top) provides new protostars (S6 and S7 in Figure 5, upper middle), making a mini-triplet system (Figure 9, bottom). The central protostar is far more massive than the companions, as in planetary systems. The mini-triplet inherits the small angular momentum of the circumstellar disk and thus has a

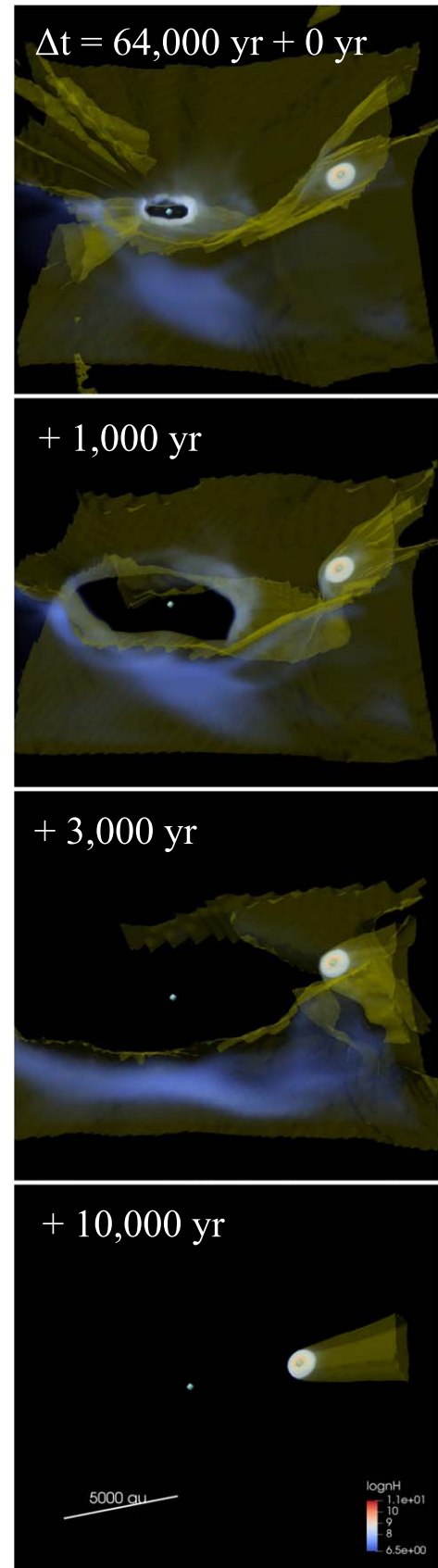


Figure 7. The external photoevaporation event shown as a time sequence in the low- \dot{M} case. From top to bottom, we show the gas (blue to red) and the ionization front (yellow) at the epochs of 0, 1000, 3000, and 10,000 yr after $\Delta t = 64,000$ yr, when the left protostar begins to completely photoevaporate its own disk from inside.

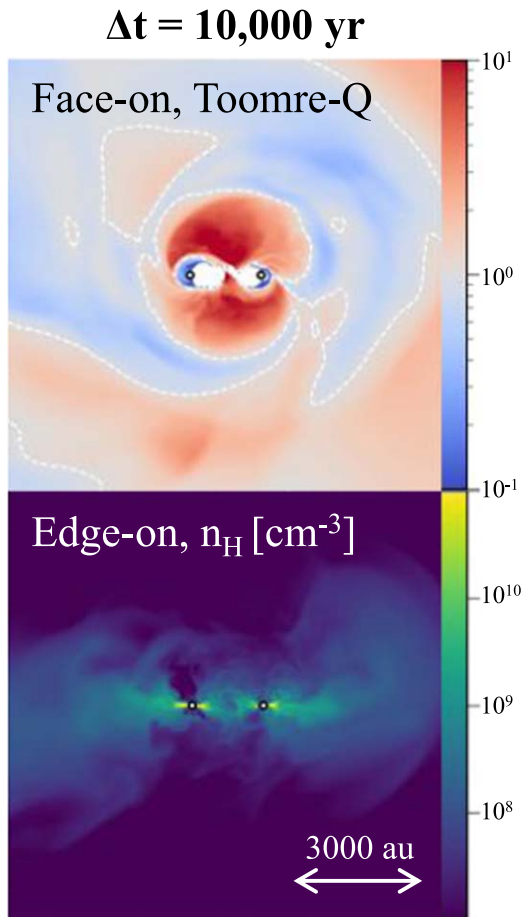


Figure 8. The Toomre’s Q parameter (top, face-on view) and number density (bottom, edge-on slice) on the scale of the circumbinary disk at $\Delta t = 10,000$ yr for the intermediate- \dot{M} case. The dashed contours in the upper panel indicate $Q = 1$, below which the disk is gravitationally unstable. The positions of the sink particles are indicated with open circles.

compact size of $\lesssim 1000$ au, in contrast to the wide outer binary at a distance of 6000 au, which carries the large angular momentum of the circumbinary disk.

Here, one circumstellar disk fragments and the other does not. Although they are similar before fragmentation ($\Delta t = 18,000$ yr), the former is slightly more unstable with a few $\times 10\%$ more mass than the other and thus causes fragmentation.

Following the formation of the mini-triplet by disk fragmentation, the gas is quickly lost in the forming stars and their subsequent accretion, which accelerates the photoevaporation of the disk (see Figure 9, bottom). The photoevaporation of the gas around the mini-triplet is completed much earlier than the counterpart in the wide outer binary, at $\Delta t = 50,000$ yr. After that, the hierarchical triplet system remains stable and shows no obvious evolution in our simulation, while the ionized region around the mini-triplet expands, reaches the other circumstellar disk, and photoevaporates it from the outside, as described in Section 3.2.1.

3.2.3. High- \dot{M} Case

In terms of event sequence, the high- \dot{M} case resembles more with the low- \dot{M} case than the intermediate- \dot{M} case. We observe initial disk fragmentation and external photoevaporation (Section 3.2.1) but do not either accretion from a circumbinary disk or late-time disk fragmentation (Section 3.2.2). As a

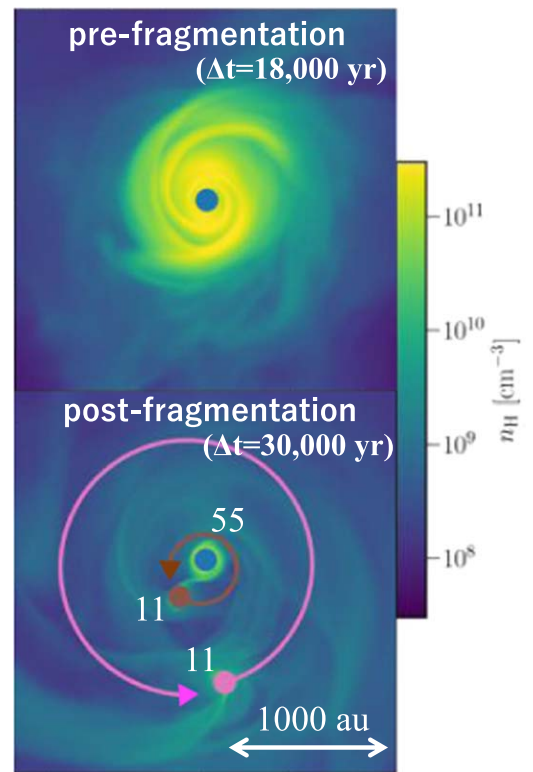


Figure 9. The density distribution of the circumstellar disk before ($\Delta t = 18,000$ yr, top) and after ($\Delta t = 30,000$ yr, bottom) fragmentation, which leads to mini-triplet formation in the intermediate- \dot{M} case. The gas distribution is shown as a face-on slice together with the sink particles marked by filled circles. In the lower panel, the trajectories of the satellites are overplotted, in the frame where the barycenter of the inner two protostars is fixed, with the masses of the protostars indicated in M_{\odot} .

process unique to the high- \dot{M} case, below we explain turbulent fragmentation preceding initial disk formation.

Turbulent fragmentation preceding disk formation—We present the gas distribution around protostars in Figure 10 at the following three stages: initial turbulent fragmentation ($\Delta t = 37$ yr), the subsequent disk formation ($\Delta t = 2000$ yr), and just before the late-time merger of the inner binary ($\Delta t = 18,000$ yr).

In the top panel, we can identify a fragment labeled with (S3) (not yet converted to a sink particle) on the upper side along a vertical filamentary structure, in addition to two protostars (S1 and S2) on the other side. Note that S2 soon merges with S1 at $\Delta t = 100$ yr and does not appear in Figure 5, which starts at $\Delta t = 1000$ yr. The turbulent fragmentation occurs only in this run, presumably because the cloud has strong turbulence and weak rotation in the initial collapse phase (Figures 1 and 2).

Eventually, the accumulation of angular momentum leads to the formation of a disk around the central protostar (S1), as shown in Figure 10 (middle). The disk subsequently becomes gravitationally unstable and undergoes fragmentation, seeding several protostars (see Figure 5, right). During the disk formation process, the gas originally belonging to the filament also accretes onto the disk. Simultaneously, the fragment, which transforms into the third sink particle (S3), is gravitationally captured by the central protostar. It then begins orbiting within the disk plane through the interactions with the disk gas, forming a close binary with ~ 300 au separation. The short separation can be attributed to the relatively low initial angular

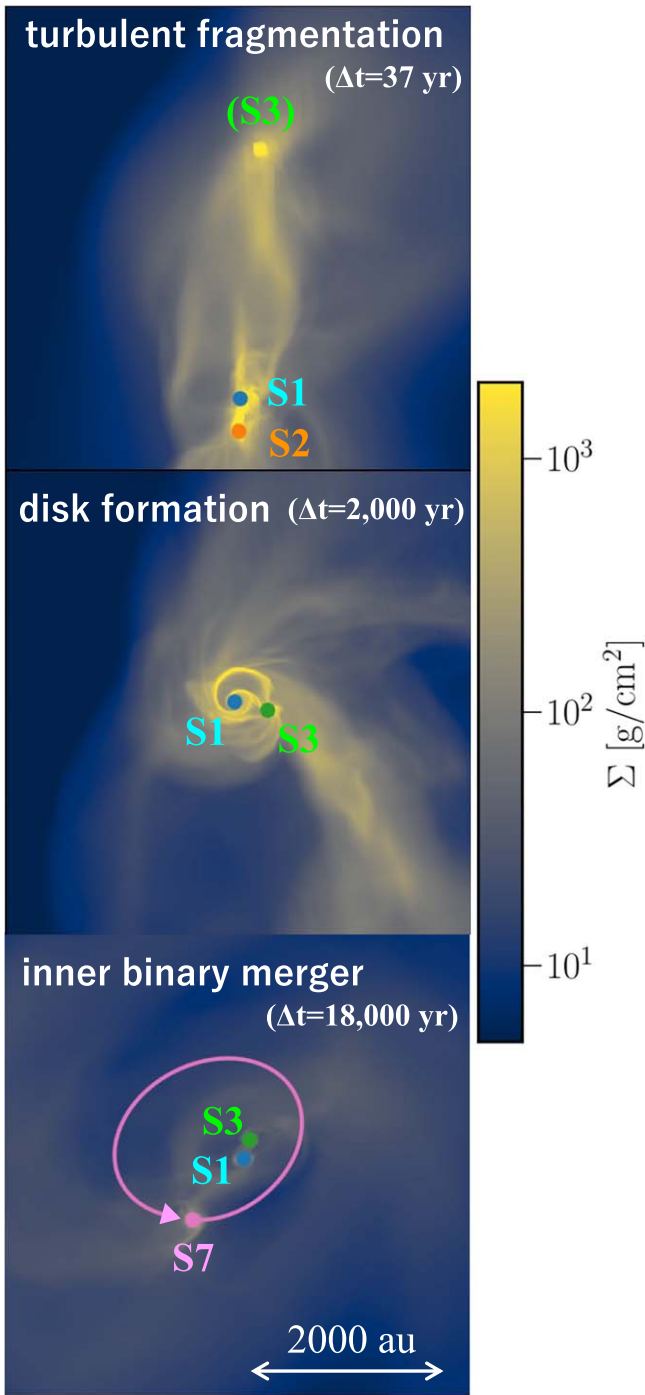


Figure 10. The time sequence of initial turbulent fragmentation ($\Delta t = 37$ yr, top), subsequent disk formation ($\Delta t = 2000$ yr, bottom), and just before the merger of the inner binary induced by a star in the outer orbit ($\Delta t = 18,000$ yr) in the high- \dot{M} case. The column density distribution is shown in the face-on view. We also show the projected positions of the sink particles with their IDs. At the epoch of the top panel, the fragment labeled with “(S3)” is yet to be converted into a sink particle. The secondary protostar, S2, in the first epoch merges with the primary, S1, and disappears before the second epoch. In the bottom panel, we show the trajectories of protostars in the frame where their barycenter is fixed. The inner binary later merges due to angular momentum extraction by the outer protostar. The axis perpendicular to each image plane is fixed in the same direction.

momentum of the protostar formed through filament fragmentation, compared with those formed through disk fragmentation.

After the disk fragmentation, many protostars merge through gravitational interaction, leaving a three-body system wherein

an outer protostar (S7) orbits an inner binary (S1–S3), as shown in Figure 10 (bottom). Soon after the epoch shown in the figure, however, the long-lasting inner binary, which originated from the capture of a filament fragment around $\Delta t \approx 2000$ yr, eventually merges due to the perturbation by S7 at $\Delta t = 20,000$ yr. This demonstrates that in a hierarchical three-body system, the outer orbit star can extract the angular momentum from the inner binary via gravitational torque and decrease its separation, rather than increasing the binary separation, as observed in the case of circumbinary disk accretion (Section 3.2.2). We here assumed that a binary has merged when the separation reaches 128 au in our criterion (see Section 2.1.1). In reality, however, our merger events could represent close binary formation below the resolution limit. This suggests the potential importance of turbulent fragmentation in close binary formation.

After the merger of the inner binary, an eccentric binary of the merger product and the outer star is left (Figure 3, lower right), similar to the low- \dot{M} case. We observe periodic modulation of the accretion rates onto the two stars with pericenter encounters of the binary in Figure 5 (Park et al. 2023). While the accretion rates modulate at the same frequency, their amplitudes are different due to the difference in the stellar gravity. The lower-mass star has the accretion rate peaking as high as $\sim 10^{-2} M_{\odot} \text{ yr}^{-1}$, which results in temporal stellar swelling and significant suppression of UV radiation (H16; Park et al. 2023; see Appendix B). Later, with a gradual decline in the peak, as well as the average, accretion rate, the UV suppression ceases.

4. Relation between the Properties of the Final Stellar System and Natal Cloud

In all three runs, we have observed the formation of massive and wide multiple star systems, with quantitative variations among them. In Section 4.1, we see the relation between properties of the final stellar systems, i.e., the total mass and binary separation, and those of initial clouds. We then discuss why Population III stars predominantly form as massive and wide multiple stellar systems based on those relations in Section 4.2.

4.1. Dependence of the Total Mass and Binary Separation on the Cloud Properties

The relation between the final stellar mass and the initial cloud-scale accretion rate has been proposed based on 2D simulations of single Population III star formation (Hirano et al. 2014). Our 3D simulations, however, have shown that multiple, rather than single, stellar systems are formed in reality. Below, we see whether a similar correlation still exists in our case.

Figure 11 shows the relation between the final total stellar mass, M_{tot} , and the initial accretion rate at the cloud scale, \dot{M}_{cloud} (see Table 1). We plot our results together with those from previous 2D axisymmetric simulations (Hirano et al. 2014) and 3D spherical grid simulations (H16). In both cases, only a single star forms in each cloud due to the numerical limitation, while accretion modulation induced by disk fragmentation is observed in the latter. We find that the total mass tends to be higher for a higher accretion rate also in our simulations, in agreement well with the fitting function

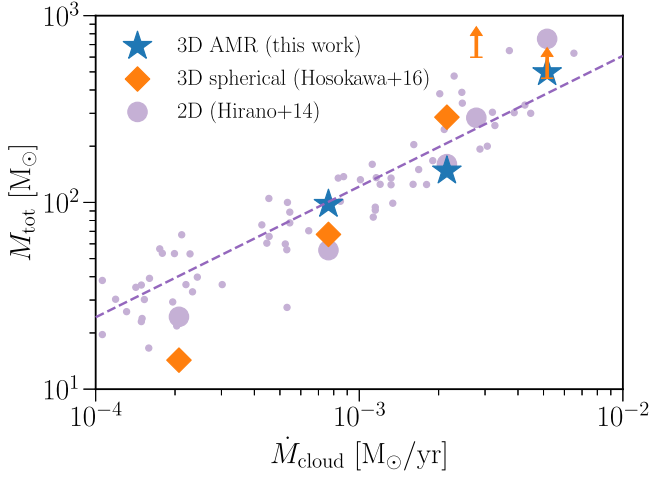


Figure 11. The relation between the final total stellar mass, M_{tot} , and the initial cloud-scale accretion rate, \dot{M}_{cloud} . We plot the data from our 3D AMR simulations (blue), along with previous 3D spherical grid simulations (H16, orange), and previous 2D simulations (Hirano et al. 2014, purple). The 2D data points are denoted by small symbols, except for those re-examined by 3D spherical grid simulations. The dashed line shows the relation proposed by Hirano et al. (2015) based on the 2D results (Equation (13)).

proposed by Hirano et al. (2015) (their Equation (7)):

$$M_{\text{tot}} = 250 M_{\odot} \times \left(\frac{\dot{M}_{\text{cloud}}}{2.8 \times 10^{-3} M_{\odot} \text{ yr}^{-1}} \right)^{0.7}. \quad (13)$$

The formation of multiple protostars has two effects on the total mass. On the one hand, mass sharing among multiple stars leads to a smaller mass of each star and thus weaker radiative feedback (see Appendix B). On the other hand, the displacement of protostars toward less dense off-centered regions leads to the suppression of accretion. In addition, the chaotic behavior of few-body systems may also introduce extra scatters in each case (e.g., Susa 2019; Wollenberg et al. 2020).

The stellar orbits also correlate with the properties of the natal clouds. Figure 12 shows the orbital angular momentum of the binaries, L_{orb} , against the corresponding initial enclosed gas angular momentum, J_{enc} . To determine these values, we first evaluate the binary’s orbital angular momentum and total mass at $\Delta t = 30,000$ yr. We then measure the initial enclosed angular momentum within the radius containing the total mass (3000, 4000, and 9000 au for the low- \dot{M} , intermediate- \dot{M} , and high- \dot{M} cases, respectively) for the cloud profile just before the formation of the first protostar (see Figure 2). Note that these radii are somewhat smaller than the cloud size, in which the cloud spin parameter λ_{cloud} is measured in Table 1. The mini-triplet in the intermediate- \dot{M} case is treated as a single object put at their barycenter. This does cause little error in evaluating the angular momentum of the system as the angular momenta of the mini-triplet’s internal orbits are negligible compared with that of the wider binary consisting of the virtual body and the other protostar.

We chose the epoch of $\Delta t = 30,000$ yr in order to eliminate the influence of radiative feedback on the binary’s orbit and focus on quantities primarily determined by the conservation laws for mass and angular momentum. By this epoch, the accretion process is nearly completed, as shown in Figure 5. As we see in the intermediate- \dot{M} case, radiative feedback possibly makes the binary’s separation change even after the end of accretion. Although some more study on the radiative feedback

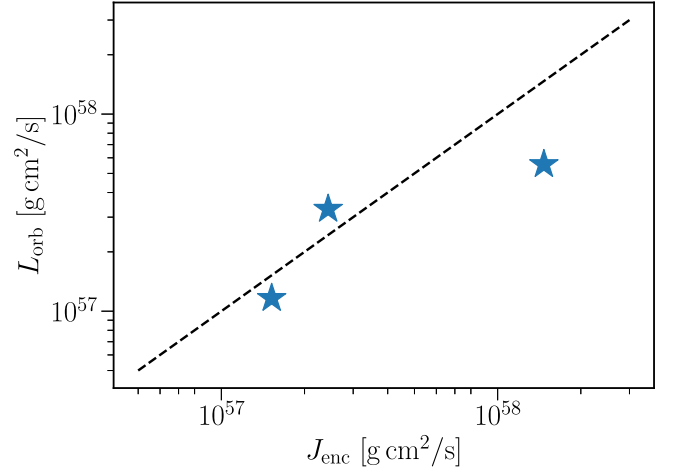


Figure 12. The relation between the angular momentum of the binary orbits, L_{orb} , and the corresponding initial enclosed angular momentum of gas clouds, J_{enc} . The binary’s orbital angular momentum and total mass are evaluated at $\Delta t = 30,000$ yr, before stellar radiative feedback drives orbital evolution. The initial enclosed angular momentum J_{enc} is calculated for the radius R_{enc} , whose enclosed mass is equal to the total mass M_{tot} , i.e., $J_{\text{enc}} \equiv J_{<R_{\text{enc}}}$ with R_{enc} satisfying $M_{<R_{\text{enc}}} = M_{\text{tot}}$. The plotted points correspond to the low- \dot{M} , intermediate- \dot{M} , and high- \dot{M} cases from left to right.

effect on the stellar orbits is needed, we speculate that its impact on the (already large) binary separation is rather limited.

Figure 12 shows that the late-time orbital angular momentum of the binary/multiple system roughly agrees with the initial angular momentum of the cloud. This means that the large angular momentum/separation of the binaries can be attributed to the large angular momentum of the clouds. Slightly lower orbital angular momentum in the high- \dot{M} case than is expected is probably due to strong turbulence in the initial cloud (Figure 2), which transfers the angular momentum outward.

4.2. Reason for Massive and Wide Multiple Star Systems

When the first protostar is still in its infancy, a disk forms around it. Being relatively massive compared with the central star, the disk easily fragments and forms multiple protostars (see Kimura et al. 2021). Such small-body systems are generally unstable by the gravitational interaction and most of them merge or are scattered away. Eventually, only a few protostars can stay within dense regions near the center and continue to grow in mass. In the following, we limit the case of binaries for simplicity although we expect a similar conclusion in few-body cases.

While the binary system gains mass by accretion from the circumbinary disk, its mass ratio approaches unity in accordance with previous dedicated studies (Bate & Bonnell 1997; Satsuka et al. 2017; Chon & Hosokawa 2019; Matsumoto et al. 2019). Note that accretion does not cause the merger of preexisting binaries: instead, it increases the binary separation (see Figure 8, bottom), rather than decreasing it (Heath & Nixon 2020; Tiede et al. 2020). Consequently, Population III stars tend to form as a system in which a few stars dominate the total mass, and presumably the total orbital angular momentum.

This system then becomes massive and wide. The total mass reaches as high as 80–500 M_{\odot} , thanks to the high cloud-scale accretion rate (Figure 11), which stems from the high temperature in the primordial gas due to the inefficient cooling (e.g., Stahler et al. 1986; Omukai & Nishi 1998).

Simultaneously, the (outer) binary has a wide orbit with its separation reaching at least 2000 au due to the large initial angular momentum of the natal cloud (Figure 12) without effective angular momentum extraction by such processes as magnetic braking or magnetically driven outflows (e.g., Machida et al. 2008a; Sadanari et al. 2021, 2023). In this way, Population III stars predominantly form as multiple systems consisting of massive stars with wide orbits.

Note, however, that this does not exclude the formation of close binaries, some of which could be progenitors of binary BH mergers observed by gravitational waves. Rather, our results have some implications for close binary formation. As in the intermediate- \dot{M} run, Population III stellar systems can be hierarchical, in which outer wide orbit stars and mini-multiplet systems coexist. Whereas the separation of the outer binary tends to increase by accretion from the circumbinary disk, stars in the outer orbit can extract the angular momentum from the inner binary and shrink its separation of the inner one, as observed in the high- \dot{M} case. Although the inner binary was regarded as merged in our simulation, the actual end product could be a close binary system below our resolution limit. A higher-resolution simulation is needed in the future to answer whether such close binaries as gravitational event progenitors are formed or not among Population III stars (e.g., Kiriara et al. 2023).

Note also that low-mass stars may still form although we have not found them in our simulations, possibly due to our limited spatial resolution and simplistic merger criteria (see also Section 5.2). Previous numerical studies on cosmological Population III star formation have suggested that numerous stars remain low mass ($<1 M_{\odot}$) after ejection from the central region of the star-forming cloud (Greif et al. 2012; Latif et al. 2022). Whether or not such stars indeed coexist in the system, however, is unlikely to significantly affect the evolution of massive protostars. Nevertheless, their formation and survival are of substantial interest from observational perspectives as current observations have already ruled out the cases where an excessive number of low-mass stars survive up to the present (Hartwig et al. 2015; Ishiyama et al. 2016).

In summary, we argue that Population III star systems are likely comprised of widely orbiting multiple massive stars. At the same time, these systems may include embedded close binaries, as well as numerous low-mass stars ejected from the center.

5. Discussion

5.1. Effect of Radiative Feedback

The radiative feedback from protostars suppresses the accretion growth of protostars, as observed in our simulations. To see how this works more specifically, here we perform a series of additional runs for the intermediate- \dot{M} case with different numerical setups. Previous authors have suggested that the accretion is suppressed either by FUV (e.g., Susa 2013; Susa et al. 2014) or EUV radiation (e.g., McKee & Tan 2008; Hosokawa et al. 2011). To discriminate the effect of each UV component, we perform runs with only FUV (no EUV) and without radiation (neither EUV nor FUV), in addition to the fiducial run both with EUV and FUV radiation. Table 3 summarizes the setups for the additional runs, along with another series of runs presented in Section 5.2.

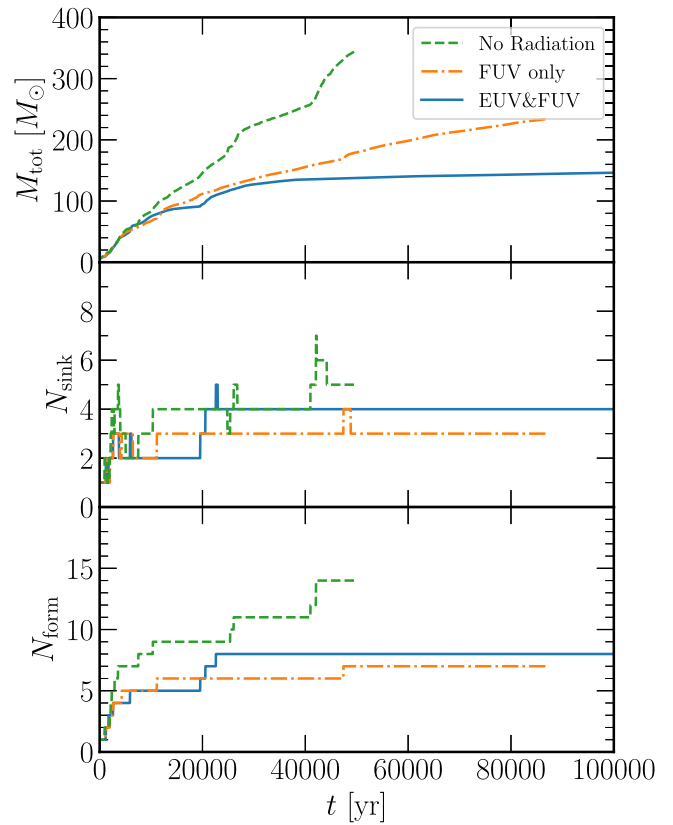


Figure 13. Dependence of protostellar evolution on the prescription of radiative feedback. From top to bottom, we plot the total mass M_{tot} , the number of surviving sinks N_{sink} , and the number of sinks formed N_{form} . The line types indicate the runs: the fiducial run with both EUV and FUV (blue solid), the FUV-only run (orange dotted-dashed lines), and the run without radiation (green-dashed lines).

Table 3
Summary of Simulation Setup for Additional Runs

Run	Δx_{min} (au)	r_{sink} (au)	n_{sink} (cm^{-3})	FUV	EUV
Int-noRad ^a	4	64	1×10^{11}	No	No
Int-noEUV ^b	4	64	1×10^{11}	Yes	No
Int-32au ^c	2	32	4×10^{11}	Yes	Yes
Int-noRad-32au ^{a,c}	2	32	4×10^{11}	No	No
Int-noRad-16au ^{a,c}	1	16	1.6×10^{12}	No	No

Notes.

^a -noRad denotes no radiation (neither EUV nor FUV).

^b -noEUV denotes no EUV (FUV only).

^c 32 and 16 au indicate the sink radius.

Figure 13 gives the comparison of the protostar evolution in the fiducial (EUV and FUV), FUV-only, and no-radiation runs. The total mass evolution (top panel) shows variation among the three runs. In the no-radiation run, the mass increases linearly at a nearly constant accretion rate without any feedback. On the other hand, in the runs with FUV radiation, the mass growth slows down due to photodissociation feedback around $\Delta t \sim 10,000$ yr. In the FUV-only run, the mass continues to grow at a reduced rate, while the EUV photoionization feedback nearly halts the accretion at $\Delta t \sim 40,000$ yr in the fiducial run with EUV. The bottom two panels in Figure 13 show the number of surviving sink particles, N_{sink} , and the total number of sinks formed, N_{form} . Due to a few-body interaction,

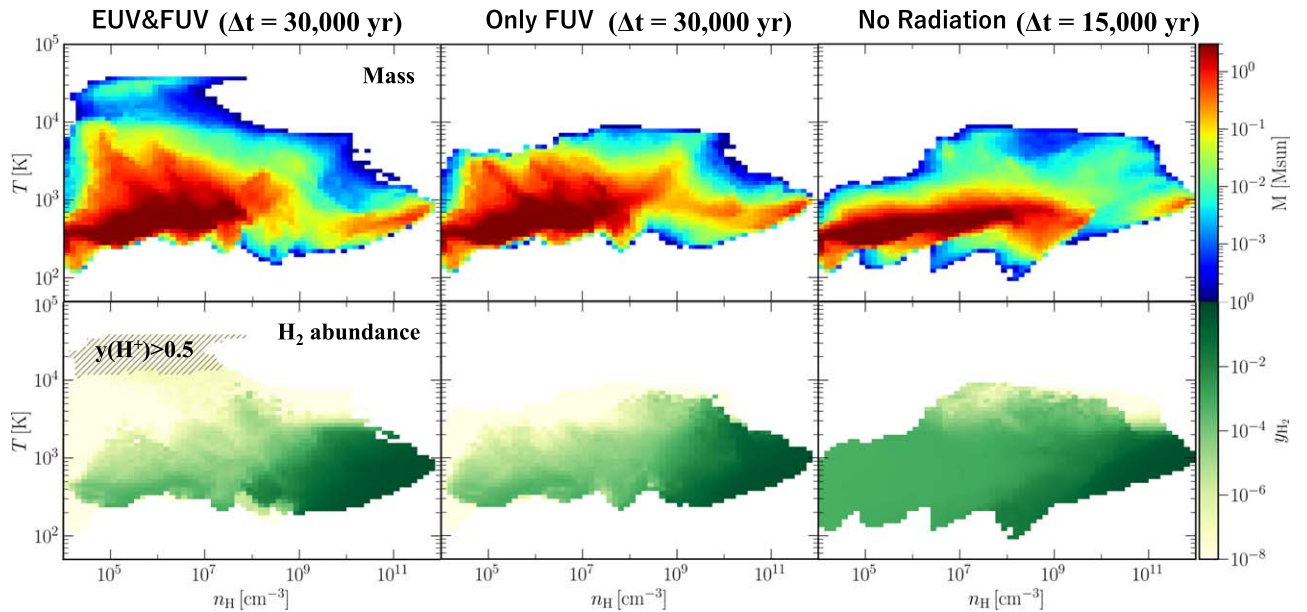


Figure 14. The density-temperature phase diagram in the fiducial run with both EUV and FUV (left), the FUV-only run (middle), and the run without radiation (right). We take the data when $M_{\text{tot}} \approx 130 M_{\odot}$ in all the runs ($\Delta t = 30,000$ yr in the first two runs and $\Delta t = 15,000$ yr in the last run). The color indicates the mass in the top row and the H_2 fraction in the bottom row. In the bottom row, hatched is the region where the gas is ionized ($y(\text{H}^+) > 0.5$).

which reduces the number of protostars through mergers, N_{sink} is similar in the range of three to five in the three runs. On the other hand, a larger difference is observed in N_{form} . While N_{form} continues to increase with time in the no-radiation run, it reaches a plateau around $\Delta t \sim 20,000$ yr in both the fiducial and FUV-only runs. This plateau is likely caused by the reduction in the accretion rate onto the disks, which falls below the rate required to sustain the formation of new sink particles through disk fragmentation.

To see how radiative feedback affects the thermal state of gases, we present density-temperature phase diagrams in Figure 14. The color in each bin represents either the mass (top) or the H_2 fraction (bottom). All the plots are for the epoch when the total mass is $130 M_{\odot}$. Around this time, FUV radiation, if included, has already suppressed the accretion and EUV radiation, again if included, begins to terminate the accretion (see Figure 13, top). The corresponding epochs are $\Delta t = 30,000$ yr in the fiducial and FUV-only runs and $\Delta t = 15,000$ yr in the no-radiation run.

The presence of FUV feedback affects the envelope gas in the density range of $10^5 - 10^9 \text{ cm}^{-3}$. A substantial portion of the gas in the envelope is heated to $T \gtrsim 1000$ K in the runs with FUV, while most of the envelope gas remains cold at $T \lesssim 1000$ K in the no-radiation run (Figure 14, top). The higher temperatures under FUV feedback can be attributed to the reduced H_2 fraction and thus cooling due to FUV photodissociation (Figure 14, bottom). The suppression of mass growth at $\Delta t \gtrsim 10,000$ yr in the runs with FUV radiation (Figure 13, top) is presumably caused by high temperature and thus pressure in the envelope.

EUV feedback leads to the formation of bipolar ionized bubbles around protostars, as depicted in Figure 4. These ionized bubbles are observed as a hot ($20,000 \text{ K} < T < 40,000 \text{ K}$) and low-density ($10^5 \text{ cm}^{-3} < n_{\text{H}} < 10^7 \text{ cm}^{-3}$) component in Figure 14. Of course, this component is observed only in the fiducial run with EUV radiation and not in the runs without EUV radiation. Consistent with previous studies (e.g., McKee & Tan 2008; Hosokawa et al. 2011), the EUV

photoevaporation of accretion disks appears to be responsible for the observed decline in accretion at $\Delta t \gtrsim 40,000$ yr in the fiducial run (Figure 13).

The analysis above highlights the distinct roles played by FUV and EUV radiation in halting the accretion. The FUV feedback starts suppressing the accretion since an early phase by quenching the main coolant H_2 , but it alone is not able to completely halt the accretion. Later on, the EUV feedback becomes active and eventually terminates the accretion by the disk photoevaporation, finally fixing the stellar mass. Given the different roles of EUV/FUV radiation in Population III star formation, we caution that ignoring either component may lead to unrealistic results.

5.2. Resolution Effects

To accelerate the computations and follow the accretion evolution to the end, we introduced sink particles. Still sink particles at finite resolution give rise to some uncertainties. Here, we assess the effect of resolution.

For this purpose, we perform additional runs for the intermediate- \dot{M} case with varying resolutions, as summarized in Table 3: two runs without radiation have two and four times higher resolution and one run with fiducial feedback model, including both EUV and FUV, has two times higher resolution. The ratio of the sink radius to the minimum cell size is fixed at $r_{\text{sink}}/\Delta x_{\text{min}} = 16$ for all runs, resulting in a sink radius of $r_{\text{sink}} = 32(16)\text{au}$ in the two (four) times higher resolution. Furthermore, we ensure that the Jeans length (proportional to $(n_{\text{sink}})^{-2}$ for a constant temperature) matches $2r_{\text{sink}}$ by increasing n_{sink} by a factor of 4 (16) when adopting two (four) times higher resolution.

Figure 15 shows the resolution dependence of sink evolution in the runs without radiation, as in Figure 13. The total mass, M_{tot} , (top panel) is consistent among runs with varying resolutions. The number of surviving sinks (middle panel) is $N_{\text{sink}} \sim 4$ due to merger in all runs while in the bottom panel, we observe a somewhat earlier rise of the total number of sinks

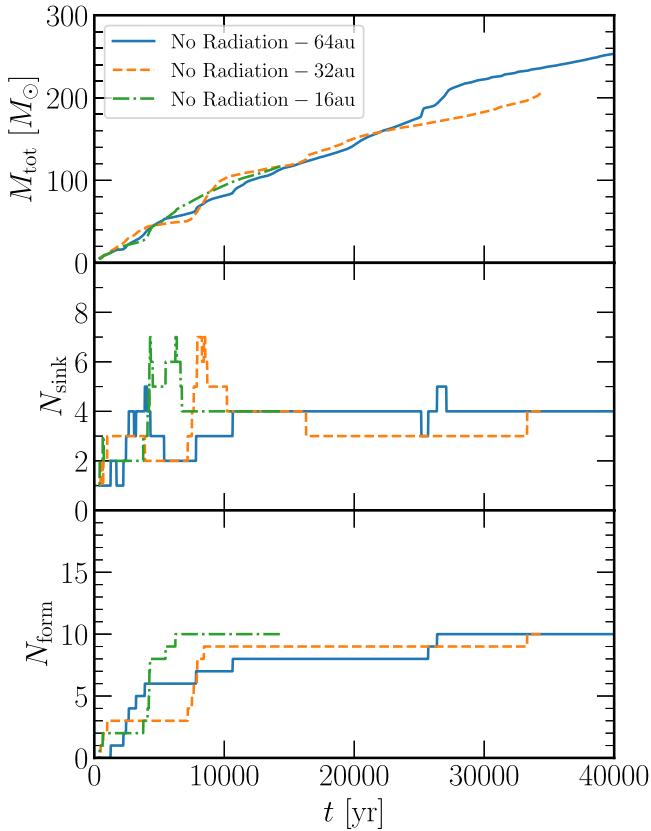


Figure 15. Same as Figure 13 but for the resolution dependence in no-radiation runs. We compare the runs with different sink radii of $r_{\text{sink}} = 64$ (blue), 32 (orange), and 16 au (green).

ever formed, N_{form} , for higher resolution runs. This can be understood from the fact that, in lower resolution runs, it takes longer for the disks to acquire enough mass for fragmentation into sinks. From the consideration above, we conclude that our results are insensitive to the resolution within the examined ranges.

Similarly, we compare the different resolution runs with radiation in Figure 16. Due to limited computational resources, it is not feasible to continue the high-resolution run beyond $\Delta t = 3 \times 10^4$ yr, despite ongoing accretion (with significant impact of radiative feedback) at this stage. Apart from the earlier rise in N_{form} in the higher-resolution run, the evolution of M_{tot} , N_{sink} , and N_{form} is in good agreement, as in the cases without radiation. This also confirms that the resolution dependence in simulations with radiative feedback is again insignificant within the examined range.

It is nonetheless plausible that some small-scale phenomena near protostars are not fully captured in our simulations. For instance, Prole et al. (2022a) reported the formation of more protostars in the initial disk fragmentation phase at higher resolution than ours. We, however, speculate that properties of massive stars would remain largely unaffected given only a few protostars can grow massive within the dense central region, as seen in Section 4.2.

Note that the sink merger criterion is linked to the resolution issue. We employ a simplified approach where two sinks are assumed to merge if their sink spheres overlap. This criterion grossly simplifies reality, and the number of surviving sinks should be viewed as a conservative lower bound. More stars,

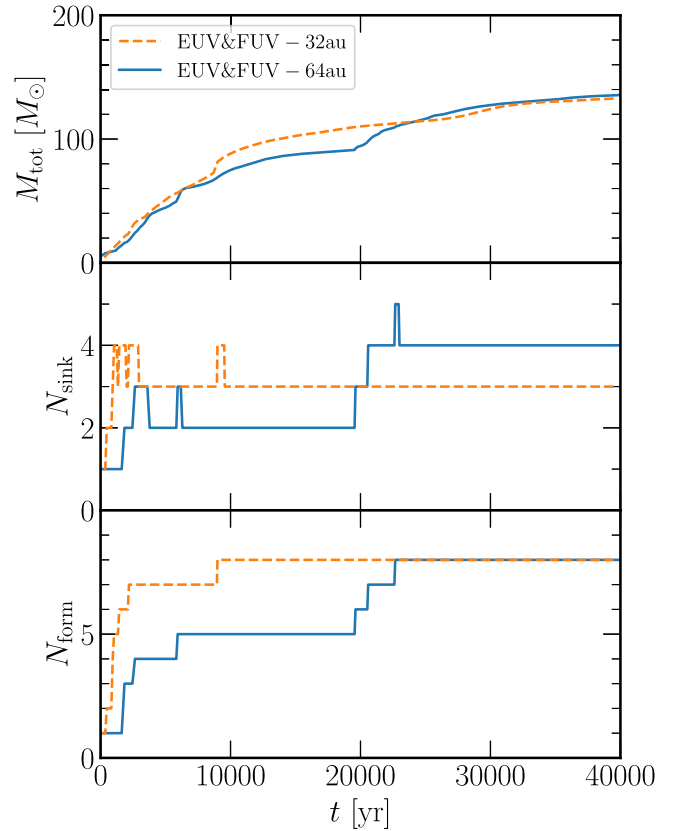


Figure 16. Same as Figure 13 but for the resolution dependence in full-feedback runs. We compare the runs with different sink radii of $r_{\text{sink}} = 64$ (blue) and 32 au (orange).

and even close binaries below our resolution, could survive all the way through the end of the accretion phase.

To eliminate all those ambiguities associated with the introduction of sink particles, it is desirable to directly resolve the protostars themselves. Although still in its infancy, such an attempt is currently underway (see Kimura et al. 2023). Nevertheless, we expect our conclusion of the formation of massive and wide binary/small multiple stellar systems to remain unchanged, as discussed in Section 4.2.

6. Summary and Conclusions

We have studied the formation of Population III stars by performing RHD simulations for three different primordial clouds extracted from cosmological hydrodynamic simulations. To accurately follow the formation of multiple protostars through gas fragmentation and their radiative feedback on the surrounding gas at a reasonable computational cost, we have developed a new code SFUMATO-RT, which employs the AMR and the ART techniques. Starting from the cloud collapse stage, we follow the growth of protostars for $\sim 10^5$ yr until their radiative feedback quenches the accretion and nearly fixes the stellar properties. Below, we summarize our findings.

1. Population III stars predominantly form as massive and wide binary/small multiple star systems in all three cases, with masses of 30–370 M_{\odot} and separations of 2×10^3 – 2×10^4 au (Section 3).
2. The properties of the formed stellar systems correlate with those of their natal clouds (Section 4.1): the total mass of the system increases with the cloud-scale

accretion rate, and the angular momentum of the binary orbit matches that of the cloud.

3. The total mass of the formed stellar system is consistent with that in previous simulations of single star formation (Hirano et al. 2014, 2015; H16). The individual masses decrease due to mass sharing among the multiple stars.
4. The reason for the formation of massive and wide binary/small multiple star systems is discussed in Section 4.2. The large total mass is due to the high accretion rate of the primordial gas, while the large angular momentum (i.e., large separation) is due to the absence of effective angular momentum transfer mechanisms via magnetic fields.
5. The following processes are identified as characteristic of Population III star formation:
 - a. A disk forms around the first protostar in the simulation. It then fragments and seeds multiple protostars. Subsequent unstable few-body interactions lead to the merger or scattering of most protostars from the central region, limiting the number of protostars that grow into massive stars. Consequently, Population III stars form as a multiple stellar system, with a few stars dominating the system's total mass.
 - b. Protostars that complete the photoevaporation of their own disks earlier than the others subsequently externally photoevaporate the disk around another protostar in their vicinity. While the impact of this process on the final stellar system requires further investigation, it may explain the observed late-time orbital evolution in one of the simulations. Moreover, external photoevaporation may influence the evolution of the Population III disk-star system, as explored in the context of present-day star formation.
 - c. When binary protostars in a circular orbit form, they accrete gas from the circumbinary disk through their respective circumstellar disks, resulting in an increase in their mass and separation due to the accretion of high angular momentum gas. The fragmentation of a circumstellar disk leads to the formation of a mini-multiple star system and accelerates the disk photoevaporation. The mini-multiple stars have shorter separations than the original wide-orbit binary stars, suggesting that the late-time fragmentation of circumstellar disks may be one of the mechanisms for the formation of short-orbit systems.
 - d. With strong initial turbulence, turbulent fragmentation occurs before disk formation. A protostar seeded by turbulent fragmentation is captured by and eventually merges with the central protostar due to its small angular momentum. The capture of stars originating from turbulent fragmentation may be another mechanism for the formation of short-orbit systems.
6. Our findings have two major implications.

First, the reduction in the individual masses of Population III stars should change their role in driving the subsequent evolution of the Universe through stellar radiation, supernovae, and seeding BHs that might rapidly grow into supermassive BHs (see, e.g., Sugimura et al. 2017, 2018; Sugimura & Ricotti 2020, and references therein). Incorporating our findings into cosmological simulations of galaxy formation is crucial for unveiling the early evolution of the Universe (see, e.g., Garcia et al. 2023).

Second, the binary Population III stars in our simulations are massive enough ($>30 M_{\odot}$) for the merger of the remnant BHs to be detectable with current gravitational wave detectors if they merge (e.g., Kinugawa et al. 2014). Their separations are too large ($\sim 1000\text{--}10,000$ au) for the remnant BHs to merge solely through the binary interaction within the present age of the Universe. However, if these binaries migrate into nuclear stellar clusters during the cosmic structure formation process, dynamical hardening can substantially accelerate the merger, as proposed by Liu & Bromm (2020) and Liu & Bromm (2021). Furthermore, our simulations suggest the possible presence of mini-binaries embedded in a wider system. Such mini-binaries may have separations short enough ($\lesssim 1$ au) for the remnant BHs to merge via binary interaction (e.g., Kinugawa et al. 2014; Tanikawa et al. 2021). In any case, further high-resolution simulations explicitly resolving such close binaries are necessary to clarify the origin of gravitational wave events.

While we have consistently treated the radiation feedback from multiple protostars, we have not considered potentially important effects, such as a magnetic field and a background radiation field. While the strength of the primordial magnetic field is still unknown, it is proposed that the magnetic field is generated and amplified by small-scale dynamo during minihalo formation (Xu et al. 2008; Schleicher et al. 2010; Sur et al. 2010; Schober et al. 2012; Turk et al. 2012; McKee et al. 2020; Stacy et al. 2022). If this is the case, we need to consider magnetic field effects in Population III formation simulations (see Machida et al. 2006; Sharda et al. 2020; Sadanari et al. 2021; Sharda et al. 2021; Prole et al. 2022b; Hirano & Machida 2022; Saad et al. 2022; Stacy et al. 2022; Sadanari et al. 2023). Some Population III stars are thought to form under the influence of radiation fields from earlier stars. Various types of radiation, including X-rays, EUV, and FUV, can affect Population III star formation (e.g., Hummel et al. 2015; Park et al. 2021a, 2021b, 2023).

The recent launch of the JWST has accelerated the observational quest into the early Universe. To prepare for the wealth of upcoming observational discoveries, it has become more urgent than ever to unveil the early cosmic history through simulations, including Population III star formation, which represents the very first step toward the formation of various objects in the Universe.

While our simulations have advanced our understanding of Population III star formation, there is a need to increase the sample size to study the diversity in Population III star formation. Furthermore, moving to higher resolutions is crucial for a more realistic depiction of Population III star formation. In our future work, we will extend our research in the direction of higher resolutions and larger sample sizes.

Acknowledgments

The authors wish to express their cordial gratitude to Prof. Takahiro Tanaka, PI of Innovative Area Grants-in-Aid for Scientific Research ‘‘Gravitational wave physics and astronomy: Genesis’’, for his continuous interest and encouragement. The authors also thank Kunihito Ioka, Jeong-Gyu Kim, Kazutaka Kimura, Masahiro Machida, Takashi Okamoto, Jongwon Park, Massimo Ricotti, Kenji Eric Sadanari, Masaru Shibata, Hajime Susa, Kengo Tomida, Masayuki Umemura, Hidenobu Yajima, and Naoki Yoshida for fruitful discussions and comments. This work would never have been accomplished without the support by MEXT/JSPS KAKENHI grant

No. 21K20373 (KS), 17H02863, 17K05394, 18H05436, 18H05437, 23K03464 (TM), 19H01934, 21H00041 (TH), 18J01296, 18H05222, 21H01123, 21K13960 (SH), and 17H01102, 17H02869, 17H06360 (KO). The numerical simulations were performed on the Cray XC50 Aterui II at CfCA of the National Astronomical Observatory of Japan, the computer cluster DRACO at Frontier Research Institute for Interdisciplinary Sciences of Tohoku University, and the Yukawa-21 at Yukawa Institute for Theoretical Physics at Kyoto University. This work is also supported by the Hakubi Project Funding of Kyoto University (KS).

Appendix A Chemical and Thermal Modeling

A.1. Chemical Network

Our chemical network is summarized in Table 4. It is the same as that in H16, except for the different treatment of H₂ photoionization. The model of H₂ photoionization has an ambiguity since H₂ direct photoionization requires an energy of at least 15.2 eV but we have only one frequency bin for EUV photons ($h\nu > 13.6$ eV). In contrast to H16, we forbid H₂ direct photoionization and allow H₂ to be photoionized by a two-step process: H₂ photodissociation H₂ + FUV \rightarrow 2 H followed by H photoionization H + EUV \rightarrow H⁺ + e.

A.2. Thermal Processes

The heating and cooling processes considered in this paper are summarized in Table 5. We add to the thermal model of

Table 4
Chemical Reactions

No.	Reactions	References
1	H + e \rightarrow H ⁺ + 2 e	1
2 ^a	H ⁺ + e \rightarrow H + γ	2
3	H ⁻ + H \rightarrow H ₂ + e	3
4	H ₂ + H ⁺ \rightarrow H ₂ ⁺ + H	4
5	H ₂ + e \rightarrow 2 H + e	4
6	H ₂ + H \rightarrow 3 H	5
7	3 H \rightarrow H ₂ + H	6
8	2 H + H ₂ \rightarrow 2 H ₂	7
9	2 H ₂ \rightarrow 2 H + H ₂	7
10	H + e \rightarrow H ⁻ + γ	4
11	H + γ \rightarrow H ⁺ + e	8
12 ^b	H ₂ + γ \rightarrow 2 H	9
13	2 H \rightarrow H ⁺ + e + H	7
14	H ⁻ + e \rightarrow H + 2 e	1
15	H ⁻ + H ⁺ \rightarrow H ₂ ⁺ + e	4
16	H ⁻ + H ⁺ \rightarrow 2 H	4
17	H ⁻ + γ \rightarrow H + e	10
18	H + H ⁺ \rightarrow H ₂ ⁺ + γ	4
19	H ₂ ⁺ + H \rightarrow H ₂ + H ⁺	4
20	H ₂ ⁺ + e \rightarrow 2 H	4
21	H ₂ ⁺ + H ⁻ \rightarrow H ₂ + H	11

Notes.

^a Case B recombination rate.

References. (1) Abel et al. (1997); (2) Glover & Jappsen (2007); (3) Kreckel et al. (2010); (4) Galli & Palla (1998); (5) Martin et al. (1996); (6) Forrey (2013); (7) Palla et al. (1983); (8) Osterbrock & Ferland (2006); (9) Draine & Bertoldi (1996); (10) John (1988); (11) Millar (1991).

Table 5
Heating and Cooling Processes

No.	Process	References
Heating		
1	H photoionization	1
Cooling		
2 ^a	H ₂ collisional excitation	2, 3
3 ^b	H ⁻ free-bound emission	4
4	H collisional ionization	5
5	H collisional excitation	5
6 ^c	Compton scattering	5
7	He ⁺ collisional excitation	5
8	H free-free emission	6
9	H free-bound emission	7
Heating/cooling		
10 ^{a,d}	Chemical heating/cooling	8, 9
11	Compression heating/expansion cooling	

Notes.

^a We calculate the line escape probability using a fitting formula provided in Fukushima et al. (2018) with the H₂ column density estimated as $N_{\text{H}_2} = \lambda_{\text{J}} n_{\text{H}} y(\text{H}_2)$.

^b We assume the average photon energy $\langle h\nu \rangle = k_{\text{B}}T + \chi_{\text{H}^-}$.

^c We assume the CMB temperature $T_{\text{CMB}} = 2.73(1+z)$ with $z = 15$.

^d The binding energies are $\chi_{\text{H}} = 13.6$ eV, $\chi_{\text{H}_2} = 4.48$ eV, and $\chi_{\text{H}^-} = 0.75$ eV (Omukai 2001).

References. (1) Osterbrock & Ferland (2006); (2) Glover (2015); (3) Fukushima et al. (2018) (4) John (1988); (5) Anninos et al. (1997); (6) Glover & Jappsen (2007); (7) Sugimura et al. (2017); (8) Hollenbach & McKee (1979); (9) Shapiro & Kang (1987).

H16 the H free-free emission and the H free-bound emission cooling. Following H16, we do not consider the H₂ CIE cooling, which is ineffective in the density range of our simulations ($n_{\text{H}} < 10^{12}$ cm⁻³), and becomes the dominant coolant only at higher densities ($n_{\text{H}} \gtrsim 10^{13}$ cm⁻³; see Omukai 2001).

Appendix B Protostar Model

We evaluate the radiation from Population III protostars using the precalculated table based on one-dimensional stellar evolution calculations (Hosokawa & Omukai 2009; Hosokawa et al. 2010). The table gives the protostellar radius R_* and luminosity L_* for a given mass M_* and accretion rate \dot{M} . Using R_* and L_* , and assuming the blackbody spectrum with the effective temperature $T_{\text{eff}} = (L_*/4\pi R_*^2 \sigma_{\text{SB}})^{1/4}$ with the Stefan-Boltzmann constant σ_{SB} , we calculate the EUV emissivity S_{EUV} and the FUV emissivity S_{FUV} as

$$S_{\text{EUV}} = 4\pi R_*^2 \int_{13.6\text{eV}}^{\infty} \frac{\pi B_{\nu}(T_{\text{eff}})}{h\nu} d\nu, \quad (\text{B1})$$

$$S_{\text{FUV}} = 4\pi R_*^2 \int_{12.4\text{eV}}^{13.6\text{eV}} \frac{\pi B_{\nu}(T_{\text{eff}})}{h\nu} d\nu. \quad (\text{B2})$$

We present our protostellar model in Figure 17.

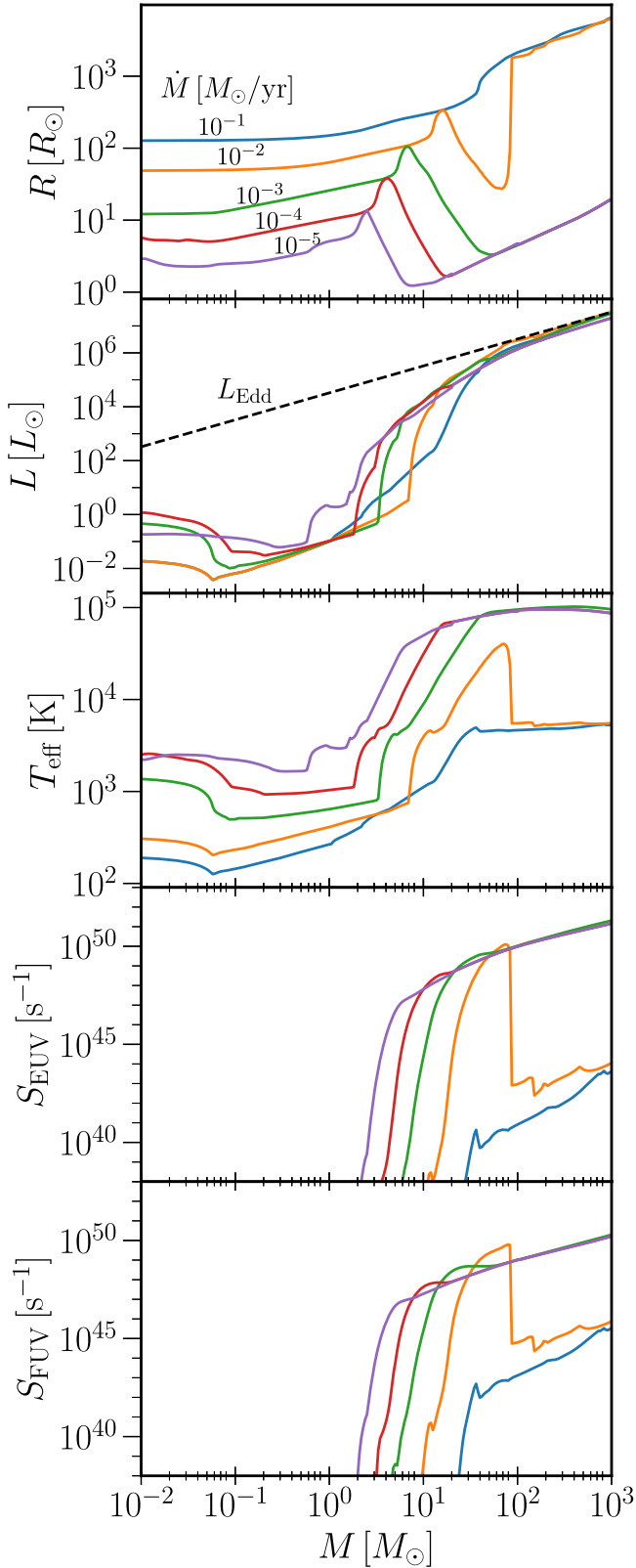


Figure 17. Radiative properties of the Population III protostars obtained from the table used in this work. We plot the protostellar radius R_* , luminosity L_* , effective temperature T_{eff} , EUV emissivity S_{EUV} , and FUV emissivity S_{FUV} from top to bottom. The horizontal axis corresponds to the mass M , and the color indicates the accretion rate $\dot{M} = 10^{-5}, 10^{-4}, 10^{-3}, 10^{-2}$, and $10^{-1} M_{\odot} \text{yr}^{-1}$ (see the labels in the top panel). In the second panel, we also show the Eddington luminosity L_{Edd} with a dashed line.

Appendix C ART Implementation

We implement an ART module on SFUMATO, following the previous implementations on other codes (Abel & Wandelt 2002; Krumholz et al. 2007; Wise & Abel 2011; Kim et al. 2017; Rosen et al. 2017). Here, we briefly review our ART implementation, optimized for SFUMATO’s oct-tree-type grid structure (see Matsumoto 2007, for details). In SFUMATO’s terminology, grids are the collection of cells (each grid has $16^3 = 4096$ cells in our simulations). Depending on a given refinement condition, each grid is refined to $2^3 = 8$ self-similar daughter grids.

In our implementation, each ray structure holds a set of variables, including the grid ID, the source ID, the direction specified by the HEALPix ID and level (see Górski et al. 2005), the distance from the source, and the optical depth in each frequency. The ray position is uniquely determined by the combination of source ID, direction, and distance. Each ray belongs to one of the CPUs. The CPU stores the ray either in the job list or in a list for sending prepared for each recipient CPU, depending on which CPU is responsible for the ray’s grid ID. The ray lists are implemented as linked lists.

When distributing a ray at a radiation source, we initialize the ray variables with its grid ID determined by searching for it from the ray position. We follow the same procedure at ray splitting, which is implemented as the annihilation of one parent ray and the generation of four daughter rays at one higher HEALPix level.

Each CPU traces rays in its job list by picking up a ray from the list one by one and advancing it. At each ray advancement, the ray passes through the cells in the grid specified by the ray’s grid ID until it reaches a grid boundary, where the ray is assigned a new grid ID corresponding to the adjacent grid to which the ray will move. After the advancement, the ray is returned to the job list if the new grid ID belongs to the same CPU or is put in a list for sending otherwise.

The rays in a list for sending are sent to the recipient CPU at some intervals. Currently, we let each CPU send rays when either its job list is empty, more than 200 rays are stored in one of the lists for sending, or 2000 times ray advancements have been made. The recipient CPU receives the rays and stores them in its job list.

To check the completion of ray tracing, we define a total job size as $N_{\text{ray,tot}} = 12 \times 2^{2l_{\text{ray,max}}}$, which is the number of rays if all rays are split to the maximum HEALPix level $l_{\text{ray,max}}$. In this work, we set $l_{\text{ray,max}} = 15$, which is large enough to ensure that rays are always split as long as the ray-splitting condition is satisfied. We terminate a ray either when it reaches a boundary of the computational box or when it is sufficiently attenuated (specifically, when $\tau_{\text{EUV}} > 100$ and $N_{\text{H}_2} > 10^{22} \text{cm}^{-2}$ ($f_{\text{shield}} < 10^{-8}$) in this work). When a ray at a level l_{ray} is terminated, the corresponding job size, $N_{\text{ray}} = 12 \times 2^{2l_{\text{ray}}}$, is added to each CPU’s job completion counter, $N_{\text{ray,cpu}}$. At some intervals, the CPUs check via MPI communication whether the sum of $N_{\text{ray,cpu}}$ over all CPUs is equal to $N_{\text{ray,tot}}$. If this is the case, the ART procedure is completed.

We have performed several tests to check the validity of our ART implementation, including tests of static and expanding H II bubbles around single radiation sources and a test of static overlapping H II bubbles around two radiation sources. All test results are physically reasonable or agree well with analytical estimates, confirming the validity of our implementation.

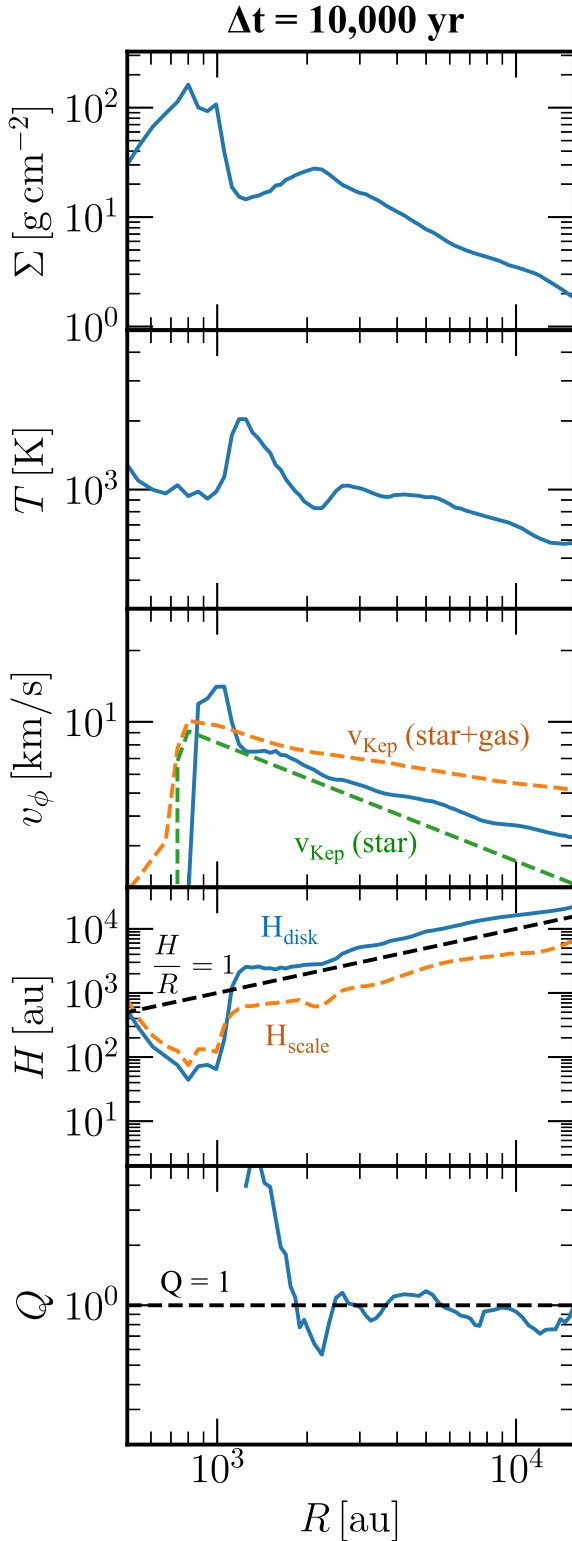


Figure 18. One-dimensional profile of the circumbinary disk presented in Figure 8. From top to bottom, we plot the angle-averaged column density Σ , temperature T , angular velocity v_ϕ , disk height H_{disk} , and scale height H_{scale} (see the text for definitions), and Toomre’s Q parameter Q . In the third panel, we show the two Kepler velocities considering only the mass of the protostars (green) and considering both the mass of the protostars and the enclosed gas mass (orange). Black-dashed lines indicate the aspect ratio of unity, $H/R = 1$, in the fourth panel and the marginally stable state, $Q = 1$, in the last panel. The two sink particles are located around 800 au from the center.

Appendix D 1D Profile of a Circumbinary Disk

To study more quantitatively the accretion flows on the scale of the circumbinary disk illustrated in Figures 3 (center), 4 (center), and 8, we present the 1D profile of angle-averaged disk quantities in Figure 18. To obtain the disk quantities, we first set the barycenter as the center and the orbital axis of the binary as the vertical axis. Then, we define the disk surface based on the heights at which the density decreases by a factor of 0.01 from the equatorial plane. Finally, we obtain disk quantities through vertical integration or averaging between the disk surfaces, depending on the variable.

The column density shown in the top panel agrees with the 2D density distribution in Figure 3 (center). It exhibits a peak around 700–1000 au, attributed to the circumstellar disks, a valley between 1000 and 2000 au resulting from the binary-induced gaps, and a gradually decreasing slope outside, corresponding to the circumbinary disk.

The second panel displays the temperature, indicating that the gas within the circumbinary disk is roughly isothermal. Enhancement near the protostars is likely a result of the radiative feedback from them.

In the third panel, we plot the rotational velocity, together with the two Keplerian velocities, considering only the mass of the protostars and considering both the mass of the protostars and the enclosed gas mass. Except for $r \sim 1500$ au, where the binary’s perturbation is significant, the rotational velocity lies between the two Keplerian velocities. This suggests that the gas self-gravity and pressure gradient play substantial roles in the radial force balance within the circumbinary disk.

The fourth panel illustrates the disk height, H_{disk} , and the scale height, $H_{\text{scale}} = c_s/\Omega$. The high pressure contributing to the radial force balance also influences the vertical force balance, causing the disk to inflate to an aspect ratio greater than unity. Note that the two heights satisfy the relation $H_{\text{disk}} \approx 3 H_{\text{scale}}$ for the hydrostatic equilibrium: the heights at which the density decreases by a factor of 0.01 is about $3 H_{\text{scale}}$ in the hydrostatic profile $\propto e^{-z^2/2 H_{\text{scale}}^2}$.

In the last panel, Toomre’s Q parameter has a marginally stable value of $Q \approx 1$ across a wide range of the circumbinary disk. This quantitatively confirms our view in Section 3.2.2 that the accretion within the circumbinary disk is driven by the self-regulated gravitational instability.

Appendix E Structure on the Scale of a Circumstellar Disk

Here, we examine the binary accretion flow on the scale of circumstellar disks. We present the 2D gas distributions in Figure 19 and the corresponding 1D profiles in Figure 20.

In Figure 19, we present the 2D snapshots around one of the circumstellar disks inside the circumbinary disk shown in Figures 3 (center), 4 (center), 8, and 18. The density (top), temperature (second), H_2 fraction (third), and H^+ fraction (last) all indicate that the gas is accreted onto the central protostar through the circumstellar disk while radiative feedback produces bipolar photoionized and photodissociated regions above and below the disk, which agrees with the (quasi-) axisymmetric case studied in the literature (e.g., Hosokawa et al. 2011; H16). The gas supply mechanism to the disk differs

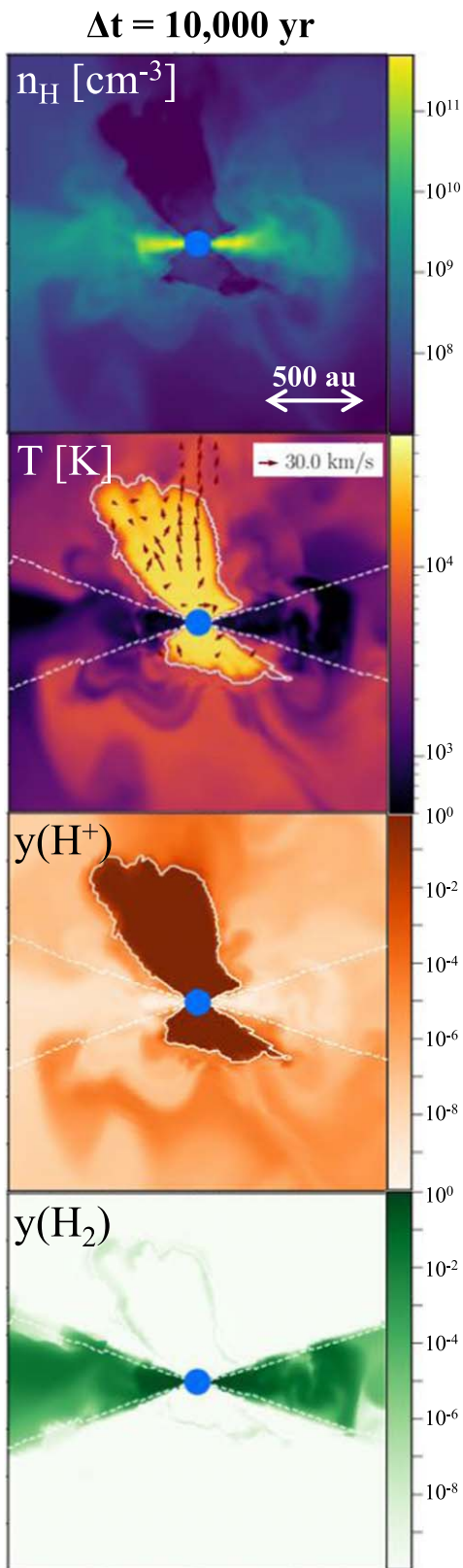


Figure 19. The edge-on slice snapshots for one of the circumstellar disks at $\Delta t = 10,000$ yr in the intermediate- \dot{M} case. From the top to bottom, we plot the density, temperature, H_2 fraction, and H^+ fraction. In the lower three panels, the bipolar photoionization and photodissociation fronts are demarcated with solid and dashed lines.

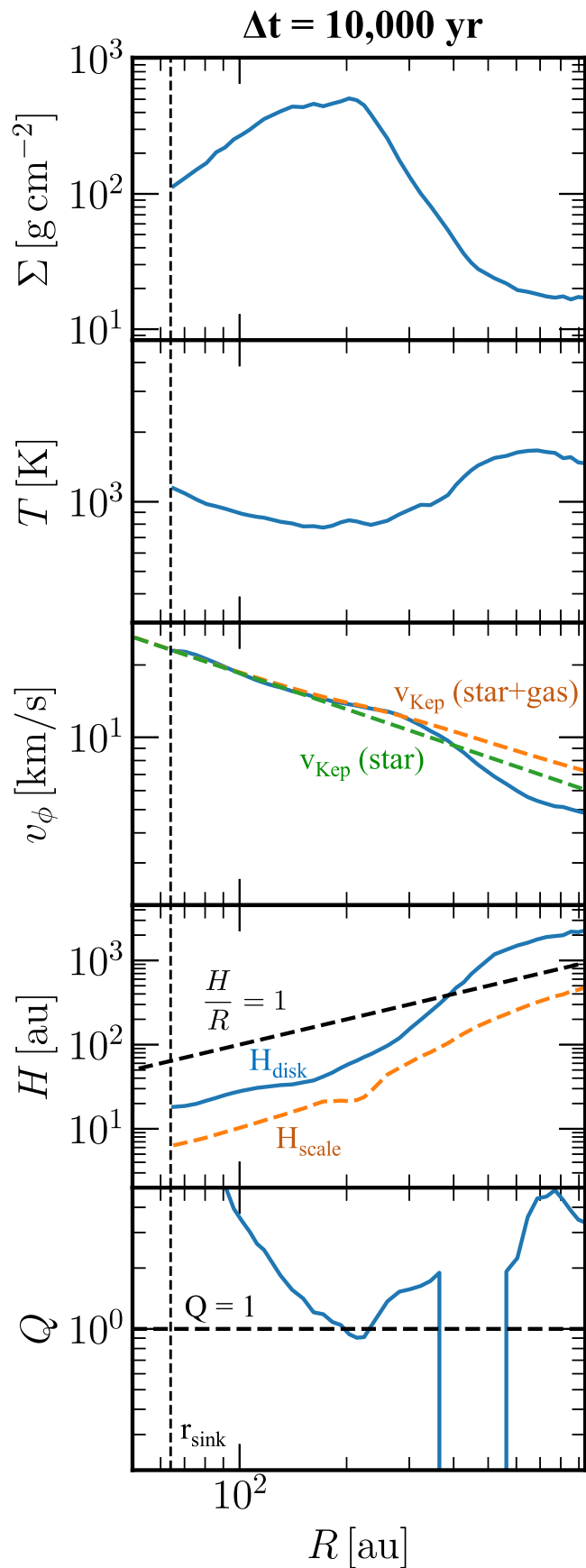


Figure 20. Same as Figure 18 but for the circumstellar disk presented in Figure 19. The sink radius is indicated with the vertical dashed line.

from the axisymmetric case, as the gas enters from one side through a bridge structure, as observed in Figure 3 (center) and explained in Section 3.2.2. However, this difference does not significantly affect the flow structure on the scale of the circumstellar disk. Therefore, the knowledge gained from single Population III star formation remains applicable in the context of binary accretion from the circumbinary disk.


Figure 20 presents the 1D profiles of the circumstellar disk illustrated in Figure 19 in the same way as in Figure 18. The surface density (top), temperature (second), rotational velocity (third), disk height (fourth), and Toomre's Q parameter (last) all agree with our understanding of disk accretion under radiative feedback, as described above. However, at this particular time ($\Delta t = 10,000$ yr), the disk is relatively small, restricting the radial range unaffected by the sink sphere ($r_{\text{sink}} = 64$ au) and the outer edge of the circumstellar disk ($r_{\text{disk}} \sim 300$ au) to a region near $r \sim 200$ au, where Toomre's Q parameter is approximately unity. In the proximity of the sink radius, the surface density decreases due to the influence of the sink particle. Near the outer edge of the disk, the pressure becomes significant, and thus the rotational velocity decreases below the Keplerian value, and the disk aspect ratio exceeds unity. We confirm that, at a later time ($\Delta t = 18,000$ yr), the disk size increases to $r_{\text{disk}} \sim 800$ au (see Figure 9, below). Consequently, a finite range of the disk is marginally stable with $Q \sim 1$, unaffected by the aforementioned effects.

ORCID iDs

Kazuyuki Sugimura  <https://orcid.org/0000-0001-7842-5488>

Tomoaki Matsumoto  <https://orcid.org/0000-0002-8125-4509>

Takashi Hosokawa  <https://orcid.org/0000-0003-3127-5982>

Shingo Hirano  <https://orcid.org/0000-0002-4317-767X>

Kazuyuki Omukai  <https://orcid.org/0000-0001-5922-180X>

References

- Abbott, B. P., Abbott, R., Abbott, T. D., et al. 2016, *PhRvL*, **116**, 061102
- Abe, M., Yajima, H., Khochfar, S., Dalla Vecchia, C., & Omukai, K. 2021, *MNRAS*, **508**, 3226
- Abel, T., Anninos, P., Zhang, Y., & Norman, M. L. 1997, *NewA*, **2**, 181
- Abel, T., Bryan, G. L., & Norman, M. L. 2002, *Sci*, **295**, 93
- Abel, T., & Wandelt, B. D. 2002, *MNRAS*, **330**, L53
- Alvarez, M. A., Wise, J. H., & Abel, T. 2009, *ApJL*, **701**, L133
- Anninos, P., Zhang, Y., Abel, T., & Norman, M. L. 1997, *NewA*, **2**, 209
- Bate, M. R., & Bonnell, I. A. 1997, *MNRAS*, **285**, 33
- Belczynski, K., Ryu, T., Perna, R., et al. 2017, *MNRAS*, **471**, 4702
- Berger, M. J., & Colella, P. 1989, *JCoPh*, **82**, 64
- Berger, M. J., & Olinger, J. 1984, *JCoPh*, **53**, 484
- Bromm, V., Coppi, P. S., & Larson, R. B. 2002, *ApJ*, **564**, 23
- Chiaki, G., Susa, H., & Hirano, S. 2018, *MNRAS*, **475**, 4378
- Chon, S., & Hosokawa, T. 2019, *MNRAS*, **488**, 2658
- Clark, P. C., Glover, S. C. O., Smith, R. J., et al. 2011, *Sci*, **331**, 1040
- Couchman, H. M. P., & Rees, M. J. 1986, *MNRAS*, **221**, 53
- Dewdney, P. E., Hall, P. J., Schilizzi, R. T., & Lazio, T. J. L. W. 2009, *IEEEP*, **97**, 1482
- Draine, B. T., & Bertoldi, F. 1996, *ApJ*, **468**, 269
- Duchêne, G., & Kraus, A. 2013, *ARA&A*, **51**, 269
- Federrath, C., Banerjee, R., Clark, P. C., & Klessen, R. S. 2010, *ApJ*, **713**, 269
- Federrath, C., Sur, S., Schleicher, D. R. G., Banerjee, R., & Klessen, R. S. 2011, *ApJ*, **731**, 62
- Forrey, R. C. 2013, *ApJL*, **773**, L25
- Fukushima, H., Omukai, K., & Hosokawa, T. 2018, *MNRAS*, **473**, 4754
- Galli, D., & Palla, F. 1998, *A&A*, **335**, 403
- García, F. A. B., Ricotti, M., Sugimura, K., & Park, J. 2023, *MNRAS*, **522**, 2495
- Glover, S. 2013, in *The First Stars*, Astrophysics and Space Science Library, ed. T. Wiklund, B. Mobasher, & V. Bromm, Vol. 396 (Berlin: Springer), 103
- Glover, S. C. O. 2015, *MNRAS*, **453**, 2901
- Glover, S. C. O., & Jappsen, A.-K. 2007, *ApJ*, **666**, 1
- Górski, K. M., Hivon, E., Banday, A. J., et al. 2005, *ApJ*, **622**, 759
- Greif, T. H. 2015, *ComAC*, **2**, 3
- Greif, T. H., Bromm, V., Clark, P. C., et al. 2012, *MNRAS*, **424**, 399
- Greif, T. H., Springel, V., White, S. D. M., et al. 2011, *ApJ*, **737**, 75
- Hartwig, T., Bromm, V., Klessen, R. S., & Glover, S. C. O. 2015, *MNRAS*, **447**, 3892
- Hartwig, T., Volonteri, M., Bromm, V., et al. 2016, *MNRAS*, **460**, L74
- Haworth, T. J., Facchini, S., Clarke, C. J., & Cleeves, L. I. 2017, *MNRAS*, **468**, L108
- Heath, R. M., & Nixon, C. J. 2020, *A&A*, **641**, A64
- Higashi, S., Susa, H., & Chiaki, G. 2021, *ApJ*, **915**, 107
- Higashi, S., Susa, H., & Chiaki, G. 2022, *ApJ*, **940**, 38
- Hirano, S., & Bromm, V. 2017, *MNRAS*, **470**, 898
- Hirano, S., Hosokawa, T., Yoshida, N., et al. 2014, *ApJ*, **781**, 60
- Hirano, S., Hosokawa, T., Yoshida, N., Omukai, K., & Yorke, H. W. 2015, *MNRAS*, **448**, 568
- Hirano, S., & Machida, M. N. 2022, *ApJL*, **935**, L16
- Hollenbach, D., & McKee, C. F. 1979, *ApJS*, **41**, 555
- Hosokawa, T., Hirano, S., Kuiper, R., et al. 2016, *ApJ*, **824**, 119
- Hosokawa, T., & Omukai, K. 2009, *ApJ*, **691**, 823
- Hosokawa, T., Omukai, K., Yoshida, N., & Yorke, H. W. 2011, *Sci*, **334**, 1250
- Hosokawa, T., Yorke, H. W., & Omukai, K. 2010, *ApJ*, **721**, 478
- Hummel, J. A., Stacy, A., Jeon, M., Oliveri, A., & Bromm, V. 2015, *MNRAS*, **453**, 4136
- Ishiyama, T., Sudo, K., Yokoi, S., et al. 2016, *ApJ*, **826**, 9
- Jaura, O., Glover, S. C. O., Wollenberg, K. M. J., et al. 2022, *MNRAS*, **512**, 116
- Jeon, M., Pawlik, A. H., Greif, T. H., et al. 2012, *ApJ*, **754**, 34
- John, T. L. 1988, *A&A*, **193**, 189
- Kim, J.-G., Kim, W.-T., Ostriker, E. C., & Skinner, M. A. 2017, *ApJ*, **851**, 93
- Kimura, K., Hosokawa, T., & Sugimura, K. 2021, *ApJ*, **911**, 52
- Kimura, K., Hosokawa, T., Sugimura, K., & Fukushima, H. 2023, *ApJ*, **950**, 184
- Kinugawa, T., Inayoshi, K., Hotokezaka, K., Nakauchi, D., & Nakamura, T. 2014, *MNRAS*, **442**, 2963
- Kirihara, T., Susa, H., Hosokawa, T., & Kinugawa, T. 2023, *ApJ*, **950**, 188
- Klessen, R. S., & Glover, S. C. O. 2023, *ARA&A*, **61**, 65
- Kreckel, H., Bruhns, H., Čížek, M., et al. 2010, *Sci*, **329**, 69
- Krumholz, M. R., Stone, J. M., & Gardiner, T. A. 2007, *ApJ*, **671**, 518
- Latif, M. A., Whalen, D., & Khochfar, S. 2022, *ApJ*, **925**, 28
- Liu, B., & Bromm, V. 2020, *ApJL*, **903**, L40
- Liu, B., & Bromm, V. 2021, *MNRAS*, **506**, 5451
- Liu, B., Meynet, G., & Bromm, V. 2021, *MNRAS*, **501**, 643
- Machida, M. N., Matsumoto, T., & Inutsuka, S.-I. 2008a, *ApJ*, **685**, 690
- Machida, M. N., Omukai, K., Matsumoto, T., & Inutsuka, S.-I. 2008b, *ApJ*, **677**, 813
- Machida, M. N., Omukai, K., Matsumoto, T., & Inutsuka, S.-I. 2006, *ApJL*, **647**, L1
- Martin, P. G., Schwarz, D. H., & Mandy, M. E. 1996, *ApJ*, **461**, 265
- Matsukoba, R., Vorobyov, E. I., Sugimura, K., et al. 2021, *MNRAS*, **500**, 4126
- Matsumoto, T. 2007, *PASJ*, **59**, 905
- Matsumoto, T., Dobashi, K., & Shimoikura, T. 2015, *ApJ*, **801**, 77
- Matsumoto, T., Saigo, K., & Takakuwa, S. 2019, *ApJ*, **871**, 36
- McKee, C. F., Stacy, A., & Li, P. S. 2020, *MNRAS*, **496**, 5528
- McKee, C. F., & Tan, J. C. 2008, *ApJ*, **681**, 771
- Millar, T. J. 1991, *A&A*, **242**, 241
- Mirabel, I. F., Dijkstra, M., Laurent, P., Loeb, A., & Pritchard, J. R. 2011, *A&A*, **528**, A149
- Moody, M. S. L., Shi, J.-M., & Stone, J. M. 2019, *ApJ*, **875**, 66
- Muñoz, D. J., Miranda, R., & Lai, D. 2019, *ApJ*, **871**, 84
- Omukai, K. 2001, *ApJ*, **546**, 635
- Omukai, K., & Inutsuka, S.-I. 2002, *MNRAS*, **332**, 59
- Omukai, K., & Nishi, R. 1998, *ApJ*, **508**, 141
- Omukai, K., & Palla, F. 2003, *ApJ*, **589**, 677
- Osterbrock, D. E., & Ferland, G. J. 2006, *Astrophysics of Gaseous Nebulae and Active Galactic Nuclei* (Sausalito, CA: Univ. Science Books)
- Palla, F., Salpeter, E. E., & Stahler, S. W. 1983, *ApJ*, **271**, 632
- Park, J., Ricotti, M., & Sugimura, K. 2021a, *MNRAS*, **508**, 6176
- Park, J., Ricotti, M., & Sugimura, K. 2021b, *MNRAS*, **508**, 6193
- Park, J., Ricotti, M., & Sugimura, K. 2023, *MNRAS*, **521**, 5334
- Park, K., & Bogdanović, T. 2017, *ApJ*, **838**, 103

- Prole, L. R., Clark, P. C., Klessen, R. S., & Glover, S. C. O. 2022a, *MNRAS*, **510**, 4019
- Prole, L. R., Clark, P. C., Klessen, R. S., Glover, S. C. O., & Pakmor, R. 2022b, *MNRAS*, **516**, 2223
- Ricotti, M. 2016, *MNRAS*, **462**, 601
- Ricotti, M., Parry, O. H., & Gnedin, N. Y. 2016, *ApJ*, **831**, 204
- Rosen, A. L., Krumholz, M. R., Oishi, J. S., Lee, A. T., & Klein, R. I. 2017, *JCoPh*, **330**, 924
- Saad, C. R., Bromm, V., & El Eid, M. 2022, *MNRAS*, **516**, 3130
- Sadanari, K. E., Omukai, K., Sugimura, K., Matsumoto, T., & Tomida, K. 2021, *MNRAS*, **505**, 4197
- Sadanari, K. E., Omukai, K., Sugimura, K., Matsumoto, T., & Tomida, K. 2023, *MNRAS*, **519**, 3076
- Satsuka, T., Tsuribe, T., Tanaka, S., & Nagamine, K. 2017, *MNRAS*, **465**, 986
- Schaerer, D. 2002, *A&A*, **382**, 28
- Schleicher, D. R. G., Banerjee, R., Sur, S., et al. 2010, *A&A*, **522**, A115
- Schober, J., Schleicher, D., Federrath, C., et al. 2012, *ApJ*, **754**, 99
- Shapiro, P. R., & Kang, H. 1987, *ApJ*, **318**, 32
- Sharda, P., Federrath, C., & Krumholz, M. R. 2020, *MNRAS*, **497**, 336
- Sharda, P., Federrath, C., Krumholz, M. R., & Schleicher, D. R. G. 2021, *MNRAS*, **503**, 2014
- Sharda, P., Krumholz, M. R., & Federrath, C. 2019, *MNRAS*, **490**, 513
- Smith, R. J., Glover, S. C. O., Clark, P. C., Greif, T., & Klessen, R. S. 2011, *MNRAS*, **414**, 3633
- Stacy, A., & Bromm, V. 2013, *MNRAS*, **433**, 1094
- Stacy, A., Bromm, V., & Lee, A. T. 2016, *MNRAS*, **462**, 1307
- Stacy, A., Greif, T. H., & Bromm, V. 2012, *MNRAS*, **422**, 290
- Stacy, A., McKee, C. F., Lee, A. T., Klein, R. I., & Li, P. S. 2022, *MNRAS*, **511**, 5042
- Stahler, S. W., Palla, F., & Salpeter, E. E. 1986, *ApJ*, **302**, 590
- Sugimura, K., Hosokawa, T., Yajima, H., Inayoshi, K., & Omukai, K. 2018, *MNRAS*, **478**, 3961
- Sugimura, K., Hosokawa, T., Yajima, H., & Omukai, K. 2017, *MNRAS*, **469**, 62
- Sugimura, K., Matsumoto, T., Hosokawa, T., Hirano, S., & Omukai, K. 2020, *ApJL*, **892**, L14
- Sugimura, K., & Ricotti, M. 2020, *MNRAS*, **495**, 2966
- Sur, S., Schleicher, D. R. G., Banerjee, R., Federrath, C., & Klessen, R. S. 2010, *ApJL*, **721**, L134
- Susa, H. 2013, *ApJ*, **773**, 185
- Susa, H. 2019, *ApJ*, **877**, 99
- Susa, H., Hasegawa, K., & Tominaga, N. 2014, *ApJ*, **792**, 32
- Tan, J. C., & McKee, C. F. 2004, *ApJ*, **603**, 383
- Tanikawa, A., Susa, H., Yoshida, T., Trani, A. A., & Kinugawa, T. 2021, *ApJ*, **910**, 30
- Tegmark, M., Silk, J., Rees, M. J., et al. 1997, *ApJ*, **474**, 1
- Tiede, C., Zrake, J., MacFadyen, A., & Haiman, Z. 2020, *ApJ*, **900**, 43
- Toyouchi, D., Hosokawa, T., Sugimura, K., & Kuiper, R. 2020, *MNRAS*, **496**, 1909
- Truelove, J. K., Klein, R. I., McKee, C. F., et al. 1997, *ApJL*, **489**, L179
- Turk, M. J., Oishi, J. S., Abel, T., & Bryan, G. L. 2012, *ApJ*, **745**, 154
- Wise, J. H., & Abel, T. 2011, *MNRAS*, **414**, 3458
- Wise, J. H., Turk, M. J., Norman, M. L., & Abel, T. 2012, *ApJ*, **745**, 50
- Wolcott-Green, J., & Haiman, Z. 2019, *MNRAS*, **484**, 2467
- Wollenberg, K. M. J., Glover, S. C. O., Clark, P. C., & Klessen, R. S. 2020, *MNRAS*, **494**, 1871
- Woosley, S. E., Heger, A., & Weaver, T. A. 2002, *RvMP*, **74**, 1015
- Xu, H., O'Shea, B. W., Collins, D. C., et al. 2008, *ApJL*, **688**, L57
- Yorke, H. W., & Welz, A. 1996, *A&A*, **315**, 555
- Yoshida, N., Omukai, K., & Hernquist, L. 2008, *Sci*, **321**, 669